Li *et al. Microstructures* **2025**, *5*, 2025003
DOI: 10.20517/microstructures.2024.69

Microstructures

Review

Open Access

Catalyst design for the electrochemical reduction of carbon dioxide: from copper nanoparticles to copper single atoms

Qianwen Li[1,2], Jingjing Jiang[2], Shanshan Jiang[3], Di Liu[2], Donghao Xu[1,2], Yongjia Chen[2], Dunru Zhu[1], Xiangwen Liu[2]

[1]State Key Laboratory of Materials-oriented Chemical Engineering, College of Chemical Engineering, Nanjing Tech University, Nanjing 211816, Jiangsu, China.
[2]Institute of Analysis and Testing, Beijing Academy of Science and Technology, Beijing 100094, China.
[3]School of Energy and Power, Jiangsu University of Science and Technology, Zhenjiang 212100, Jiangsu, China.

Correspondence to: Prof. Dunru Zhu, State Key Laboratory of Materials-oriented Chemical Engineering, College of Chemical Engineering, Nanjing Tech University, No. 30 Puzhu South Road, Nanjing 211816, Jiangsu, China. E-mail: zhudr@njtech.edu.cn; Prof. Xiangwen Liu, Institute of Analysis and Testing, Beijing Academy of Science and Technology, No. 27, West 3rd Ring Rd North, Beike Building, Beijing 100094, China. E-mail: liuxiangwen@bcpca.ac.cn

How to cite this article: Li, Q.; Jiang, J.; Jiang, S.; Liu, D.; Xu, D.; Chen, Y.; Zhu, D.; Liu, X. Catalyst design for the electrochemical reduction of carbon dioxide: from copper nanoparticles to copper single atoms. *Microstructures* **2025**, *5*, 2025003. https://dx.doi.org/10.20517/microstructures.2024.69

Received: 5 Aug 2024 **First Decision:** 18 Oct 2024 **Revised:** 25 Oct 2024 **Accepted:** 1 Nov 2024 **Published:** 18 Jan 2025

Academic Editors: Dingsheng Wang, Zaiping Guo **Copy Editor:** Ping Zhang **Production Editor:** Ping Zhang

Abstract

Carbon dioxide reduction reaction (CO_2RR) is an efficacious method to mitigate carbon emissions and simultaneously convert CO_2 into high-value carbon products. The efficiency of CO_2RR depends on the development of highly active and selective catalysts. Copper (Cu)-based catalysts can effectively reduce CO_2 to hydrocarbons and oxygen-containing compounds because of their unique geometric and electronic structures. Most importantly, Cu can reduce CO_2 to multiple carbon products (C_{2+}). Therefore, this review aims to outline recent research progress in Cu-based catalysts for CO_2RR. After introducing the mechanism of this electroreduction reaction, we summarize the influence of the size, morphology, and coordination environment of single component Cu-based catalysts on their performance, especially the performance control of catalysts that contain nano Cu or Cu single-atom sites. Then, the synergistic regulation strategies of doping other metals into Cu-based catalysts are summarized. Finally, the research on the supports used for Cu-based catalysts is reviewed. The prospects and challenges of Cu-based catalysts are discussed.

Keywords: CO_2RR, copper, nanoparticles, single atoms, electrocatalyst

INTRODUCTION

The world is currently facing a severe energy crisis. The problems of air pollution, plastic pollution, water pollution, and carbon dioxide (CO_2) emissions become increasingly serious and need to be urgently addressed[1-3]. In the past century, the concentration of CO_2 has increased due to rapid energy consumption, leading to serious global warming problems[4]. At present, many methods have been proposed to alleviate climate change, including the capture and sequestration of CO_2, which is still a big challenge due to the relative chemical inertness of CO_2[5]. Among them, the electrochemical method can convert CO_2 into more valuable carbon products[6-8]. Metal catalysts, such as Au, Ag, Cu, Pd, *etc.*, can effectively reduce CO_2. Cu-based catalysts are the focus because they can efficiently catalyze CO_2 into multiple carbon products[9]. The formation of $*C_2$ intermediates requires sufficient surface CO_2 concentration and $*C_1$ coverage. However, since these intermediates need to be able to move freely, the adsorption strength of the catalyst used for $*C_1$ intermediates should not be too high. Cu has moderate adsorption strength for these intermediates, so it is considered to be the most favorable heterogeneous catalyst for the electroreduction of CO_2[10-15]. Although Cu has a high binding strength to *CO, it has disadvantages of high overpotential and low selectivity for C_{2+} products, such as ethylene (C_2H_4), ethanol (CH_3CH_2OH), acetic acid (CH_3COOH), acetone (CH_3COCH_3) and propanol ($CH_3CH_2CH_2OH$)[16,17].

In 1870, it was first discovered that CO_2 could be electro-reduced to formic acid (HCOOH) in aqueous media[18,19]. In 1985, Hori *et al.* were the first person to observe that Cu can reduce CO_2 to methane (CH_4) and C_2H_4[20]. In particular, C_2H_4 is only produced on Cu electrodes. They found that the selectivity of CH_4 and C_2H_4 is related to the pH and cation of the electrolyte. A higher pH value is conducive to the formation of C_2H_4, and the selectivity of C_2H_4 improves with the increase in cation size[21,22]. Since then, many researchers have conducted research on Cu-based catalysts for the reduction reaction of CO_2 (CO_2RR).

Improving the selectivity of Cu-based catalysts to CO_2RR products is a current research focus. However, due to the wide variety of CO_2RR reaction pathways and product types, the high-selective formation of a certain product is challenging. Cu-based electrocatalysts have made significant progress as key materials for CO_2RR technology in recent years. Modifying Cu-based catalysts by doping or changing crystal planes, sizes, and morphologies can affect the bonding strength of important electroreduction intermediates such as *CO and *OCHO, which enables to improve the function of Cu-based catalysts. In addition, electrolytes and applied currents can alter the structure of Cu-based catalyst, causing changes in catalytic performance. In recent years, many researchers have found that the selectivity of Cu-based catalysts to certain reduction products in CO_2RR can be effectively improved through nanoconfinement effects, composite catalysts, introducing hydrophilic metals, and increasing surface hydrophobicity of catalysts.

This article reviews recently important progress on Cu-based catalysts for CO_2RR. Firstly, the synergistic control strategies of the morphology, size, and chemical environment of single-component Cu-based catalysts and their effects on catalyst performance are discussed based on the active components of the catalysts, especially the performance control of nano Cu and Cu single-atom sites. Subsequently, the synergistic regulation strategies of Cu-based catalysts doped with other metals are summarized. Finally, the supports of Cu-based catalysts are summed up. Additionally, prospects and challenges are discussed.

REACTION MECHANISM OF CO_2RR

The catalytic processes of CO_2RR typically involve the following three steps[6]:

(1) CO_2 first adsorbs on the catalyst, forming $*CO_2$[19,23];

(2) The transfer of electrons and protons causes the dissociation of C=O bonds, resulting in the formation of C-H and C-O bonds;

(3) Product desorbs from the catalyst surface[24].

At the thermodynamic level, transferring the first electron to the CO_2 molecule requires large recombination energy (750 kJ mol^{-1}) to activate CO_2[25,26]. On Cu, CO is a key intermediate for CO_2RR to produce hydrocarbons[27].

As shown in Figure 1, the different pathways of CO_2RR reactions result in the production of various intermediate products, such as C_1, C_2, and C_3, and involve multi-electron or proton transfer[28].

Table 1 lists the semi-reactions of different products and their standard reduction potentials relative to reversible hydrogen electrodes (RHE) under alkaline conditions[28,29]. Among them, the hydrogen evolution reaction (HER) is a competitive reaction[30-33]. However, a variety of products are usually detected on the surface of Cu, resulting in poor selectivity of products. Moreover, competitive HER and inefficient *CO dimerization in aqueous solution still limit the performance of CO_2RR[34]. Therefore, it is necessary to regulate the selectivity and suppress HER through various means, e.g., by regulating catalyst morphology, adding additives, and modifying the catalyst surface.

SINGLE-COMPONENT CU-BASED CATALYSTS

The active components of a catalyst refer to the species that play a catalytic role in the catalyst. At present, transition metals are mainly the active component of CO_2RR catalysts. As shown in Figure 2, metals can be divided into four categories according to surface-bound intermediates[35]. Ni, Fe, Pt, and Ti easily catalyze H_2 formation via HER during the CO_2RR process[36]. The surfaces of Au, Ag, Zn, and Pd mainly produce CO[37]. Pb, In, Sn, and other metals preferably generate HCOOH[25,38-40]. Cu can further reduce the intermediate *CO in the CO_2RR process to produce high-value carbon products[35,41-44]. Accordingly, Cu is the focus of many researchers. In this section, we mainly summarized some representative Cu-based nanoparticles (NPs) and single-atom catalysts (SACs), the control functions of additives for Cu-based catalysts to regulate CO_2RR catalysis, and the corresponding selective catalytic mechanisms.

Cu nanoparticles

Cu NPs refer to the catalysts with size of Cu particles in the nanometer range. The size, morphology, chemical environment, and crystal plane of Cu NPs have a significant influence on the products and performance of CO_2RR. When the size of Cu particles decreases to the nanometer level[45,46], the catalyst exhibits higher surface activity and richer surface defects than the Cu particles with larger sizes[47-49]. The surface properties and structures of Cu NPs can be regulated by appropriate synthesis methods[50]. Thus, the selectivity and activity of the catalytic reaction can be adjusted[51]. Modifying the surface of Cu NPs with hydrophobic materials, such as Nafion[52,53], polytetrafluoroethylene (PTFE)[54], and alkyl thiol[55], can inhibit HER and promote CO_2 mass transfer[56,57], thereby improving the efficiency of CO_2RR and enhancing C_{2+} selectivity. Cu NPs are attractive catalysts for CO_2RR to produce valuable chemicals[58]. Next, we will summarize some Cu NP catalysts with different morphologies, sizes, and chemical environments to regulate the catalytic effect of CO_2RR and the corresponding selective catalytic mechanism.

Table 1. The semi-reactions of CO_2RR and their standard reduction potentials *versus* RHE

Products	Equation	Potential (V)
H_2	$2H_2O + 2e^- \rightarrow H_2 + 2OH^-$	-0.828
CO	$CO_2 + 2H_2O + 2e^- \rightarrow CO + 2OH^-$	-0.932
HCOOH	$CO_2 + H_2O + 2e^- \rightarrow HCOO^- + OH^-$	-0.639
CH_3OH	$CO_2 + 5H_2O + 6e^- \rightarrow CH_3OH + 6OH^-$	-0.812
CH_4	$CO_2 + 6H_2O + 8e^- \rightarrow CH_4 + 8OH^-$	-0.659
C_2H_4	$2CO_2 + 8H_2O + 12e^- \rightarrow C_2H_4 + 12OH^-$	-0.743
C_2H_6	$2CO_2 + 10H_2O + 14e^- \rightarrow C_2H_6 + 14OH^-$	-0.685
CH_3CH_2OH	$2CO_2 + 9H_2O + 12e^- \rightarrow CH_3CH_2OH + 12OH^-$	-0.744
CH_3CHO	$2CO_2 + 7H_2O + 10e^- \rightarrow CH_3CHO + 10OH^-$	-0.775
CH_3COOH	$2CO_2 + 5H_2O + 8e^- \rightarrow CH_3COO^- + 7OH^-$	-0.653
n-C_3H_7OH	$3CO_2 + 13H_2O + 18e^- \rightarrow$ n-$C_3H_7OH + 18OH^-$	-0.733
CH_3COCH_3	$3CO_2 + 11H_2O + 16e^- \rightarrow CH_3COCH_3 + 16OH^-$	-0.726

Reproduced with permission[29]. Copyright 2023, Springer Nature. CO_2RR: Carbon dioxide reduction reaction; RHE: Reversible hydrogen electrode.

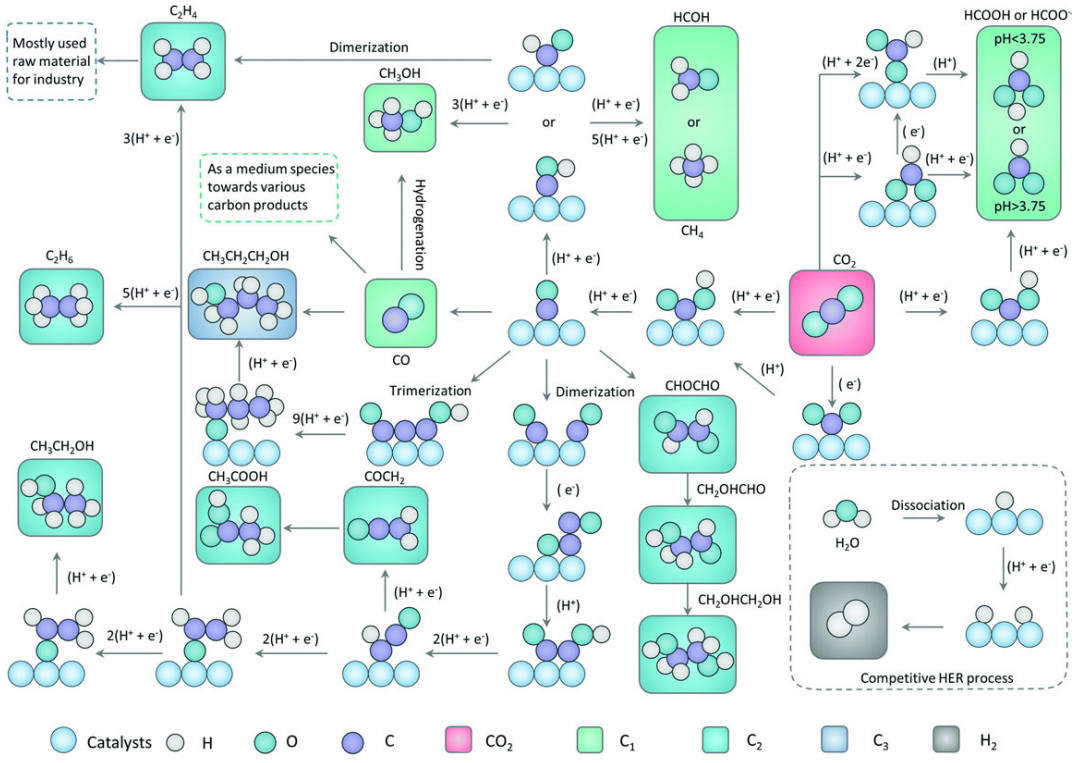

Figure 1. Possible mechanistic pathways of ECO_2RR towards C_1 and C_2 products. (Reproduced with permission[19]. Copyright 2022, Royal Society of Chemistry). ECO_2RR: Electrocatalytic reduction of CO_2.

Reske *et al.* synthesized six spherical Cu NP catalysts of different average sizes (2-15 nm) and coordination numbers (CNs) by stirring $CuCl_2$ loaded micelles and changing the molecular weight of polyvinylpyrrolidone (PVP) heads or metal salt/PVP ratios [Figure 3A-F][59]. As shown in Figure 3G and H, the proportion of atoms with low CNs (Cu-CNs < 8) significantly increased in Cu NPs with particle sizes less than 6 nm. During CO_2RR, the catalytic activity increased but tended to promote HER, mainly producing H_2 and CO. Manthiram *et al.* prepared Cu NPs with a diameter of 7.0 ± 0.4 nm terminated with

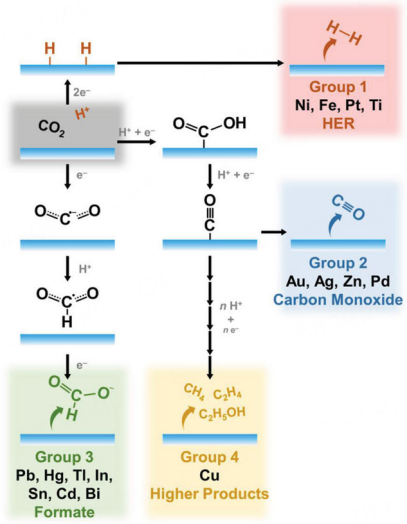

Figure 2. The classification of metal catalysts for CO_2 reduction. (Reproduced with permission[35]. Copyright 2020, Wiley Materials).

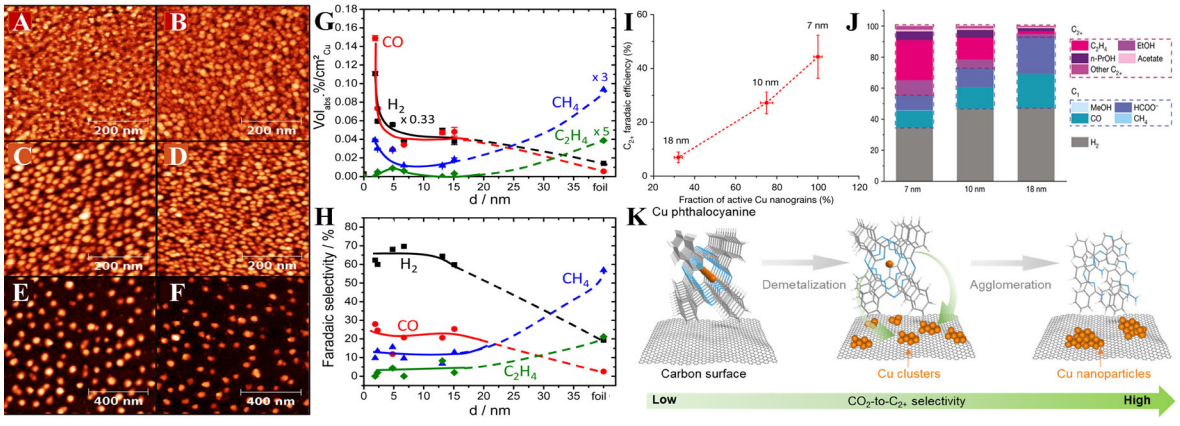

Figure 3. (A-F) Tapping-mode AFM images of micellar Cu NPs; Particle size dependence of (G) the composition of gaseous reaction products (balance is CO_2) during catalytic CO_2 electroreduction over Cu NPs; (H) the faradic selectivities of reaction products during the CO_2 electroreduction on Cu NPs. (Reproduced with permission[59]. Copyright 2014, American Chemical Society); (I) Structure-activity correlation of relative fraction of active Cu nanograins and C_{2+} FE of Cu NP ensembles with three different NP sizes; (J) FE for all CO_2RR products of three different Cu NP sizes (7, 10 and 18 nm) at -0.8 V. (Reproduced with permission[62]. Copyright 2023, The Author(s), under exclusive license to Springer Nature Limited); (K) Structure-activity correlation of relative fraction of active Cu nanograins and C_{2+} FE of Cu NP ensembles with three different NP sizes.(Reproduced with permission[63]. Copyright 2023, American Chemical Society). NPs: Nanoparticles; CO_2RR: Carbon dioxide reduction reaction; FE: Faraday efficiency; AFM: Atomic force microscopy.

tetradecyl phosphonate by reducing cupric acetate $Cu(Ac)_2$ in trioctylamine[60]. The Faraday efficiency (FE) of CH_4 is 76% at -1.35 V *vs.* RHE. The current density of CH_4 was four times that of Cu foil electrodes. They found that more isolated NPs exposed more catalytic active sites to form CH_4. However, when the Cu NPs aggregated, CH_4 would be lost in the products. Jung *et al.* prepared a 20 nm Cu_2O NP/C with cubic morphology. Cu NPs were grown on the carbon carrier using cysteine molecules[61]. Under negative potential, the 20 nm cubic Cu_2O crystal particles disintegrated into 2-4 nm particles, and FEs of C_2H_4 (FE of C_2H_4) and C_{2+} (FE C_{2+}) of the shattered Cu-based NP/C catalyst reached 57.3% and 74%, respectively. Yang *et al.* reduced $Cu(Ac)_2$ precursors with tetradecyl phosphonic acid at high temperatures to prepare Cu NPs, and controlled the size of Cu NPs by adjusting the ratio[62]. The authors established that

the selectivity of C_{2+} increased with the proportion of metallic Cu nanograins. The 7 nm Cu NP with a unity fraction of Cu nanograins exhibited six times higher FE C_{2+} than the 18 nm Cu NP ensemble with one-third of Cu nanograins [Figure 3I and J]. As shown in Figure 3K, Zhang *et al.* adsorbed a mixture of Cu phthalocyanine (CuPc) and carbon black (CB) onto a glassy carbon wafer and electroreduced CuPc to Cu NPs (20 nm) under CO_2RR conditions[63]. The size of Cu NPs was influenced by the reaction time, reduction potential, oxidation degree of the carbon support, and the loading amount of CuPc. Furthermore, due to the abundance of grain boundaries in large NPs, the selectivity of C_{2+} products also increased from 0% to 40% during the slow growth of Cu NPs (2 nm to 20 nm). The highest FE C_{2+} was 70%, and the current density for C_{2+} was 800 mA cm^{-2}.

Cu NPs with various morphologies and crystal faces have different effects on CO_2RR. Zi *et al.* found that Cu nanoneedles can induce ultra-high local potassium concentration (4.22 M)[64]. High concentrations of potassium can promote the C-C coupling, achieving efficient CO_2 reduction in 3-M KCl electrolytes of pH = 1. FE C_{2+} reached up to 90.69% ± 2.15% at 1,400 mA cm^{-2}. Fu *et al.* prepared a series of Cu_2O nanocrystals (NCs) with diverse crystal faces and morphologies[65]. Among them, the o-Cu_2O NCs with high-index facets reached the highest FE C_{2+} (48.3%). They investigated the structural alterations of Cu_2O NCs after stability tests and discovered that abundant crystal defects and high-index facets were observed, which may be the active sites. As shown in Figure 4A, Luo *et al.* modified the surface of Cu_2O particles using reducing agents[66], and found that the star-shaped Cu_2O NPs (F-Cu_2O) with exposed (322) facets achieved the highest C_2H_4 selectivity (FE = 74.1%). They found that the Cu_2O (332) surface can significantly reduce the free energy during the coupling process of *CHO intermediates and promote the production of C_2H_4. As shown in Figure 4B, they further modified the surface with ZIF-8. The ZIF-8 shell provided abundant pores, substance exchange channels and appropriate hydrophobic microenvironments, which facilitated the desorption of *CO intermediates. Periasamy *et al.* prepared stable Cu_2O/polypyrrole (Cu_2O/Ppy) particles on linen-textured (LT) paper[67]. The Cu_2O/Ppy with octahedral and micro flower shapes had exposed (111) facets, (311) and (211) facets, exhibiting high selectivity towards CH_3OH products. At -0.85 V *vs.* RHE, the FE of methanol (FE of CH_3OH) was 93% ± 1.2%. Wu *et al.* prepared a highly stable mixed Cu_2O-Cu nanocube catalyst [Cu_2O (CO)] by thermal reduction of CuO nanocubes under CO atmosphere[68]. The material exhibited a high-density CuO/Cu interface and abundant Cu (100) crystal planes. At an industrial current density of 500 mA cm^{-2}, the FE of C_{2+} products was 77.4% (FE of C_2H_4 was 56.6%). Recently, as shown in Figure 4C-E, Geng *et al.* prepared hydrophobic porous Cu_2O spheres (pore sizes 140/240/340 nm) using polystyrene (PS) spheres as pore guides by wet chemical methods[69]. The hydrophobic porous morphology of the catalyst facilitated the transportation and capture of CO_2 and promoted CO_2 activation and the formation of *OCCOH intermediates, thereby promoting C-C coupling. The P-Cu_2O-240 sample had the highest CO_2 mass transfer efficiency. As shown in Figure 4E, at -1.0 A cm^{-2}, FE C_2 was 75.3% ± 3.1%.

The grain boundaries of Cu NPs affect the selectivity of CO_2RR. Frese *et al.* first discovered an increase in CH_4 production on Cu (100), Cu (110), and Cu (111)[70]. Hori *et al.* found that Cu (100) and Cu (111) tended to generate C_2H_4 and CH_4, respectively, while Cu (110) preferably produced acetate and acetaldehyde. They also reported that CO is a key intermediate in CO_2RR[71]. Schouten *et al.* observed that the Cu (100) surface tended to form C_2H_4 at a relatively low overpotential, while the Cu (111) surface preferentially generated CH_4 and only a small amount of C_2H_4[72]. Gao *et al.* found that the crystal facets exposed by Cu_2O NPs greatly affected the selectivity of CO_2-C_2H_4 [Figure 5A-F][73]. Cu_2O NPs with both (111) and (100) crystal faces demonstrated a stronger selectivity for CO_2-C_2H_4 with an FE of C_2H_4 of 59% compared to Cu_2O NPs with only one crystal face. Wu *et al.* further proved this point[74]. They found that the Cu (100)/Cu (111) interface had a good localized electronic structure, which enhanced CO adsorption and C-C coupling, and its performance was better than that of the Cu (100) and Cu (111). Ma *et al.*

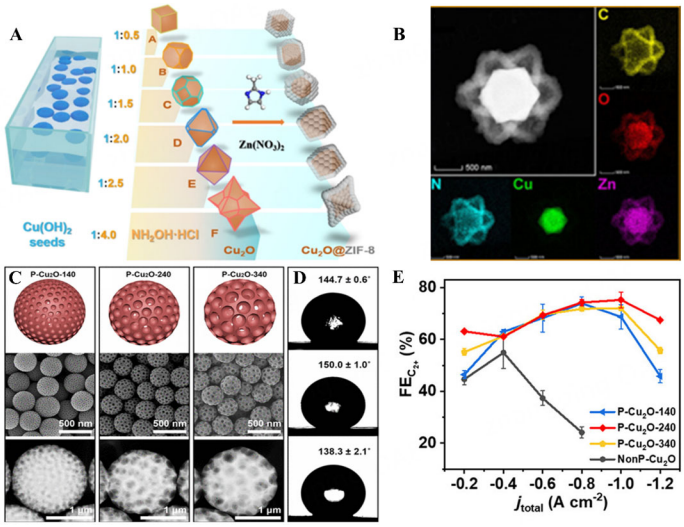

Figure 4. (A) Synthesis of Cu_2O NPs by the reductant-controlling method and Cu_2O@ZIF-8 composites; (B) HAADF-STEM image and elemental mappings. (Reproduced with permission[66]. Copyright 2022, Wiley-VCH GmbH); (C) Scheme, SEM, and enlarged HAADF-STEM images of P-Cu_2O-140, P-Cu_2O-240, and P-Cu_2O-340; (D) Water contact angle (CA) of P-Cu_2O-140, P-Cu_2O-240, P-Cu_2O-340 (from top to bottom); (E) FEs for C_{2+} products under different applied current densities over porous Cu_2O samples. (Reproduced with permission[69]. Copyright 2024, American Chemical Society). NPs: Nanoparticles; HAADF-STEM: High-angle annular dark-field scanning transmission electron microscopy; FE: Faraday efficiency.

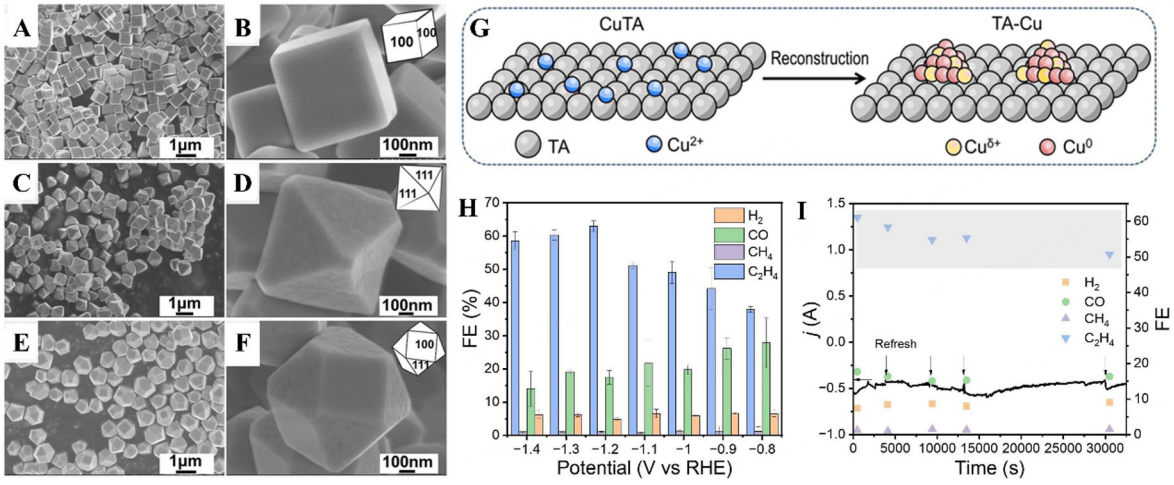

Figure 5. SEM images of (A, B) c-Cu_2O NPs; (C, D) o-Cu_2O NPs; and (E, F) t-Cu_2O NPs. (Reproduced with permission[73]. Copyright 2020, WILEY-VCH Verlag GmbH & Co. KGaA, Weinheim); (G) The preparation of TA-Cu via electrochemical reconstruction of CuTA; (H) FEs of TA-Cu obtained at different applied potentials; (I) Stability for CO_2 electrolysis with the TA-Cu. (Reproduced with permission[76]. Copyright 2023, Wiley-VCH GmbH). NPs: Nanoparticles; TA: Tannic acid ; FE: Faraday efficiency; SEM: Scanning electron microscope.

reconstructed Cu NPs on vertical graphene [plasma-enhanced chemical vapor deposition (PECVD)][75]. They constructed incompatible sites and abundant oxygen vacancies on Cu active sites through reduction-oxidation-reduction (ROR), enhancing CO_2RR activity. This catalyst had abundant grain boundaries, producing *COOH-derived products (CO) at high oxidation potentials (+1.2 V *vs.* RHE), and *OCHO-derived products (HCOOH) at low oxidation potentials (+0.8 V *vs.* RHE). Recently, Chen *et al.* utilized tannic acid (TA) molecules *in situ* to regulate and reconstruct Cu-based materials and prepared a Cu electrocatalyst (TA-Cu)[76]. Cu (111) NPs and partially oxidized CuO_x were uniformly distributed on

TA-Cu nanorods [Figure 5G]. The hydroxyl groups in TA could stabilize the key intermediate *COH through hydrogen bonding, thereby promoting the generation of C_2H_4. At -0.7 V *vs.* RHE, the process reached an FE of C_2H_4 of 63.6%, a stability of ten h, and a current density exceeding 497.2 mA cm^{-2} [Figure 5H and I].

Carbon intermediates can be effectively limited by forming nano-sized confined spaces in Cu-based materials, thus effectively promoting the formation of C_{2+}. For example, Liu *et al.* prepared a porous Cu nanosphere catalyst (P-Cu)[77], which can enrich the intermediate *CO in the pore structure. As shown in Figure 6A-C, Zhang *et al.* found a volcano curve relationship between the selectivity of C_2H_5OH and the nanocavity size of porous CuO in the range of 0 to 20 nm[78]. The increase in *OH coverage associated with the nanocavity size-dependent confinement effect was believed to account for the remarkable CH_3CH_2OH selectivity. Increased *OH coverage may facilitate the hydrogenation of *CHCOH to *CHCHOH (CH_3CH_2OH pathway). As shown in Figure 6D and E, p-CuO-(12.5 nm) has an FE of CH_3CH_2OH of 44.1% ± 1.0% at a high C_2H_5OH partial current density of 501.0 ± 15.0 mA cm^{-2}, while FE C_{2+} was 90.6% ± 3.4%. Liu *et al.* increased the coverage of local CO by introducing a Cu hollow multi-shell structure (HoMSs) and utilizing the nano-constrained effect[79]. The presence of Cu in the cavity stabilized *CO and promoted dimerization. As the shell layer increased, the selectivity and activity of C_{2+} products significantly improved. The Cu HoMSs with three shells exhibited the largest FE C_{2+} in neutral electrolyte of 77.0% ± 0.3%, and the current density was 513.7 ± 0.7 mA cm^{-2}. As shown in Figure 6F-H, based on mature CO_2-CO electroreduction technology, Yang *et al.* reported porous Cu_2O catalysts with nanocavities[80]. They found that fragmented and solid Cu_2O catalysts mainly produced CO, while the FE of C_{2+} production on porous Cu_2O catalysts was much higher, indicating that the porous structure could promote C-C bonding. At -0.61 V *vs.* RHE, the FE C_{2+} was 75.2% ± 2.7%, and the partial current density was 267 ± 13 mA cm^{-2}. They found that pore cavities could restrict the *in-situ* generation of carbon intermediates effectively, which bound with Cu sites [Figure 6I]. In addition, this restricted intermediate promoted C-C coupling within the reactive nanocavity.

Modifying the Cu NPs with different materials can enhance C-C coupling, thereby improving the production of multiple carbon products. For example, Zhao *et al.* reported an *in-situ* polymerization strategy of encapsulating hydrophobic polymers onto Cu NPs to synthesize fluorinated polymer-functionalized Cu NPs (Cu poly-1/2)[58]. Increasing the hydrophobicity of the catalyst surface can suppress HER, which is beneficial for reducing the thickness of the CO_2 gas diffusion layer and promoting CO_2 mass transfer[56,57]. Compared with bare Cu (FE C_{2+} = 61.59%), the use of Cu poly-1/2 increased the FE C_{2+} to 71.08% at -3.98 V *vs.* RHE. Pellessier *et al.* covered commercial Cu NPs with porous PTFE nanocoats[54]. The physical adsorption of PTFE on Cu NPs generated a large interface surface area, which could improve the binding energy of CO intermediates on Cu and enhance C-C coupling. The FE C_{2+} was 78% within the current density range of 400-500 mA cm^{-2}. Using ammonia and $Cu(NO_3)_2$ as raw materials, Zhou *et al.* prepared AN-$Cu(OH)_2$ by a one-step wet chemical method. Then, the acidic ionomer Nafion was used to regulate the surface hydrophobicity and local alkalinity of the catalyst [AN-Cu(OH)@Nafion][52]. The FE of C_2H_4 of optimal Nafion-activated AN-Cu(OH)@Nafion was 44%, and HER was effectively inhibited. Recently, Su *et al.* used Nafion to modify Cu NP catalyst (Cu@Nafion)[53]. Nafion can inhibit HER and enhance CO_2 mass transfer, which is beneficial for C-C coupling. At -1.2V *vs.* RHE, FE C_{2+} was about 73.5%, and HER decreased from 40.6% to 16.8%. As shown in Figure 7A and B, Chen *et al.* developed a Cu polyamine hybrid catalyst by co-electroplating polyamines onto the surface of Cu electrodes (Cu-Pi, i =1-5)[81]. The amine functional group causes higher pH values and has higher intermediate stability, as well as the ability to adsorb more CO, thereby improving the selectivity of C_2H_4. The Cu-P1 catalyst reached the highest FE of C_2H_4 of 72%. As shown in Figure 7C and D, Lin *et al.* modified

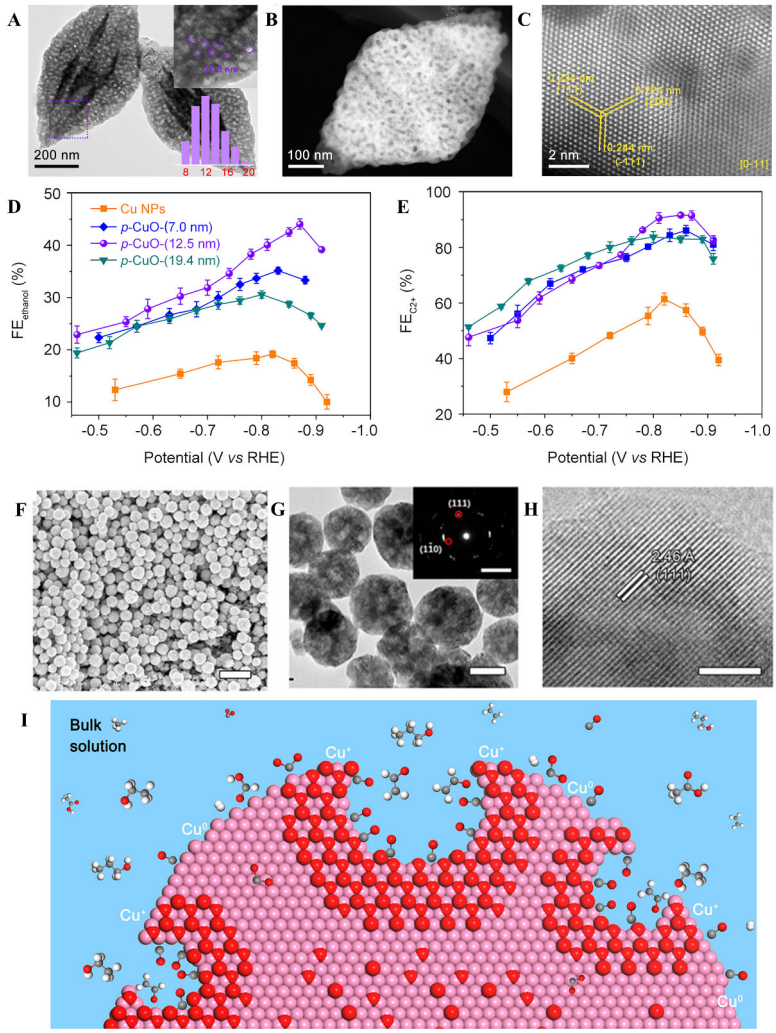

Figure 6. (A) TEM images of *p*-CuO-(12.5 nm); (B) HAADF-STEM images of *p*-CuO-(12.5 nm); (C) High-resolution HAADF-STEM images of *p*-CuO-(12.5 nm); (D) $FE_{ethanol}$ and (E) FE C_{2+} over Cu NPs, *p*-CuO-(7.0 nm), *p*-CuO-(12.5 nm), and *p*-CuO-(19.4 nm) catalysts. (Reproduced with permission[78]. Copyright 2023, PNAS); Multihollow Cu_2O catalyst imaged by SEM (F), TEM (G) and HRTEM (H); The inset in (G) shows the corresponding SAED pattern; (I) Schematic of carbon intermediates that are confined in the nanocavities. White: H; gray: C; red: O; violet: Cu. (Reproduced with permission[80]. Copyright 2020, American Chemical Society). HAADF-STEM: High-angle annular dark-field scanning transmission electron microscopy; NPs: Nanoparticles; FE: Faraday efficiency; TEM: Transmission electron microscope; HAADF-STEM: High-angle annular dark-field scanning transmission electron microscope; HRTEM: High-resolution transmission electron microscope; SAED: Selected-area electron diffraction.

alkyl thiols with different alkyl chain lengths to regulate the interfacial wettability[55]. The FE C_{2+} of the Cu-12C catalyst was the highest, reaching 86.1%. At 400 mA cm^{-2}, the catalyst achieved an FE C_{2+} of 80.3% [Figure 7E and F], which is one of the best performances at this current density. Increasing the interfacial hydrophobicity of the catalyst effectively prevented the absorption of H_2O, facilitated CO_2 transportation, increased *CO coverage, and thus enhanced C_{2+} selectivity[82].

The above results indicate that enhancing the C-C coupling process in CO_2RR is significant for the formation of C_{2+} products, and the efficiency depends on the coverage of *CO intermediates on the catalyst surface. For smaller-sized Cu-based NPs, adjusting the chemical environment of catalytically active sites can adjust the adsorption capacity for *CO, while for slightly larger catalyst particles, the adsorption capacity of

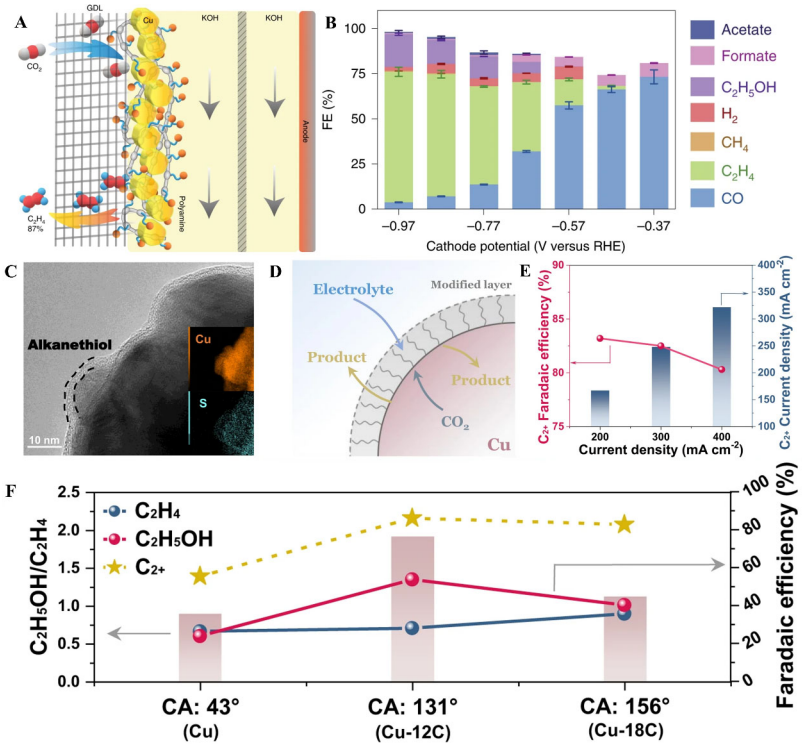

Figure 7. (A) Schematic illustration of P1 and Cu co-electroplating on the GDL; (B) FE for all products on Cu-P1. [Reproduced with permission[81] .Copyright 2020, The Author(s), under exclusive license to Springer Nature Limited]; (C) HRTEM image of Cu-12C, revealing a 2-3 nm continuous and conformal alkanethiol layer; (D) Illustration shows Cu catalysts via hydrophobic treatment by alkanethiol; (E) FE and partial current densities of C_{2+} on Cu-12C under different current densities; (F) The variety of product selectivity with different interfacial wettability. [Reproduced with permission[55].Copyright 2023, The Author(s)]. FE: Faraday efficiency; GDL: Gas diffusion layer; HRTEM: High-resolution transmission electron microscope.

*CO can be adjusted through nano-confined-space strategies. Enhancing the concentration of *CO can effectively promote the formation of C_{2+} products. Modifying the surface of Cu NPs with different materials will influence the selectivity of CO_2RR products. When using hydrophobic materials, HER can be suppressed, thereby enhancing the CO_2 reduction efficiency. When modified with hydrophilic salt materials, C_1 products can be promoted, thereby reducing the generation of C_{2+}. The synthesis of nanocavity structures using nanoconfinement effects can enrich and stabilize CO, greatly increasing the concentration of CO on Cu NPs and promoting the generation of C_{2+} products. Adjusting the Cu surface through different molecules is beneficial for reducing the energy barrier of C-C coupling and stabilizing intermediates, thereby improving CO_2RR performance. However, the stability of Cu NPs is generally poor, and using appropriate carriers to anchor Cu NPs and developing new synthesis strategies are feasible methods to increase stability.

Cu-based single atoms

In Cu-based SACs, Cu atoms exist in the form of single atoms and can effectively participate in the reaction process. SACs have maximum atomic utilization efficiency and high catalytic activity[83], and can promote the catalytic reaction[84]. Compared with other Cu-based catalysts, Cu SACs have a higher utilization rate of active sites[85]. These SACs can maximize the utilization of Cu resources through reasonable design and preparation methods[86]. Due to their monodispersed catalytic sites, some Cu SACs cannot overcome the energy barrier of C-C coupling, inhibiting such reactions and thereby the formation of C_{2+} products and improving the selectivity of C_1 products such as CH_4, CO, CH_3OH, and HCOOH[87,88]. The key to improving

the performance of SACs is to regulate the interaction between catalytically active sites and reaction intermediates[89]. The CO_2RR performance of Cu SACs can be improved by precisely adjusting the coordination environment and electronic structure of the central metal[90,91]. Most single-atom Cu is loaded onto C-based or NC materials through coordination with C or N. A strong correlation exists between catalytic activity and the coordination environment (such as CN and coordinating atoms) of Cu metal centers[92]. For example, Cu-C and Cu-N can promote the generation of CH_4 and CO, respectively, and Cu-N_2, Cu-N_3 and Cu-N_4 also form different catalytic effects. Metal and nitrogen-doped carbon (MNC) catalyst can activate and reduce CO_2 to various products. The separation of electrons and geometric sites of a single metal atom will make the poor adsorption of H, thus eliminating the Tafel-type reaction and inhibiting the HER effectively[93]. In this section, we will summarize in detail the impact of the coordination environment of Cu SACs on their performance in CO_2RR.

When Cu SACs coordinate with C in graphene to form Cu-C bonds, the activation sites of CO_2 molecules are changed to promote the formation of *OCHO intermediates, thereby promoting the production of CH_4[94-98]. In the process of CO_2RR, the Cu-C bond formed by loading Cu atoms on carbon materials is usually conducive to the formation of *OCHO, which is converted to CH_4. Shi *et al.* immobilized Cu single atoms on graphdiyne (GDY) and constructed Cu-C bonds for the first time[99], which not only stabilized the single Cu atoms but also enhanced the electronic control effect. They found that the Cu-C bond could induce the formation of *OCHO. Furthermore, the catalyst had a stronger binding ability to CO_2 than H_2O, thus suppressing HER. The maximum FE of CH_4 was 81% at a stable electroreduction of ten h. Zhao *et al.* prepared Cu SACs with Cu-C_2 coordination structure by accurately anchoring single Cu atoms onto hydrogenated graphdiyne (HGDY), using the special structure of 1,3,5-triethynylbenzene through the Sonokashira reaction Cu single atoms (Cu-SAs)/HGDY[98]. They confirmed that the low-coordination Cu-C_2 provided the Cu single-atom center with more positive charges and promoted the formation of H• and improved the selectivity of CH_4. At -1.1 V *vs.* RHE, FE of CH_4 was 44%, and the CH_4 current density was 230.7 mA cm^{-2}. Importantly, the catalyst achieved a turnover frequency (TOF) of 2,756 h^{-1}.

When Cu coordinates with N in graphite carbon nitride (*g*-C_3N_4), it tends to produce CH_4[100], and it can stabilize Cu single atoms[99]. Li *et al.* incorporated single-atom Cu into the nitrogen cavity of the host *g*-C_3N_4[100]. The catalyst exhibited an FE of CH_4 of 49.04% and a maximum CH_4/C_2H_4 ratio of 35.03. The Cu-N-C structure enhances the adsorption of *COOH and promotes the desorption of *CO, which is beneficial for the production of CO. Chen *et al.* anchored single-atom Cu onto a carbon nitride structure (Cu-N-C)[101], which enhanced the adsorption of *COOH and promoted the desorption of *CO. A high FE of CO of 98% with a local current density of 131.3 mA cm^{-2} was achieved at -0.67 V *vs.* RHE. Cai *et al.* prepared a carbon dot-supported SAC (Cu-CDs) with a unique CuN_2O_2 site [Figure 8A-E][87]. Since the generation of hydrocarbons requires to transfer more electrons and thereby a higher energy barrier, the product of CO_2RR is usually CO. Therefore, the authors used partial carbonization to adjust the electronic structure of the Cu atom, thus reducing the total endothermic energy of *OCHO. Due to the introduction of oxygen ligands, FE of CH_4 increased to 78% [Figure 8F and G]. Furthermore, they believed that pyridinic N was the anchor site for CO_2 capture, due to the oxidation of Cu^{2+} in Cu-CD which had more pyridinic N than CD. Atomic-dispersed Cu-N_3-C catalysts also exhibit excellent selectivity for CO. Chen *et al.* used biomass guanosine to directly synthesize a two-dimensional (2D) atom-dispersed Cu-N_3-C catalyst (CuG-1000)[102]. The electrons were transferred from Cu coordinated with N to *COOH, thus regulating the adsorption and desorption of key intermediates and improving the selectivity of CO. At -0.65 V *vs.* RHE, the FE of CO of CuG-1000 reached 99% with a current density of 6.53 mA cm^{-2}. Recently, as shown in Figure 8H-K, Purbia *et al.* synthesized Cu-SAC-N-doped carbon quantum dots (Cu SAC-N-CQDs) catalysts using $CuCl_2$ as the Cu source and dopamine hydrochloride as the carrier through a hydrothermal

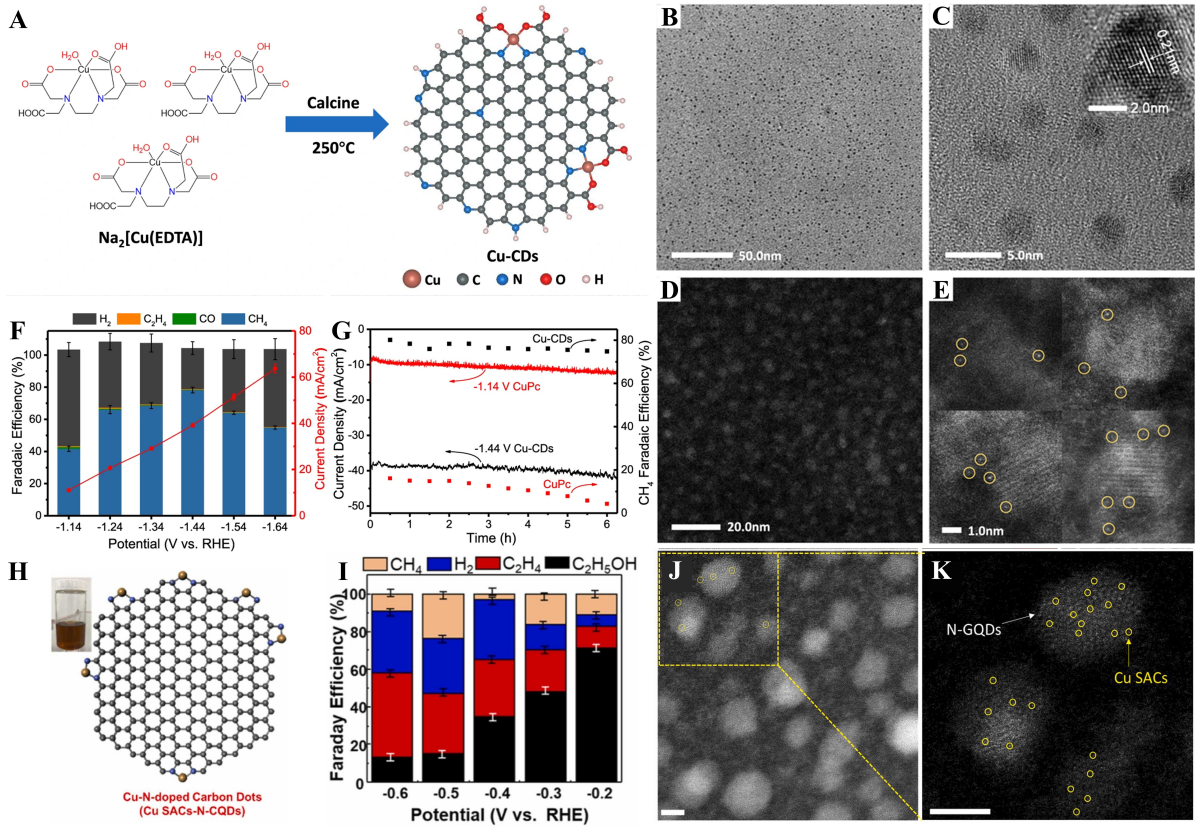

Figure 8. (A) Scheme of the low-temperature calcining procedure for Cu-CD catalysts; (B) Large-field of view and (C) magnified view of TEM images; (D) Relatively large-field of view and e typical view of HAADF-STEM images of distributed single Cu atoms in carbon dots. Yellow circles in (E) indicate typical single Cu atoms; (F) FE and current density of Cu-CDs; (G) Stability test of Cu-CDs and CuPc at their highest ECR FE potentials. [Reproduced with permission[87]. Copyright 2021, The Author(s)]; (H) Structural schematic diagram of Cu SACs N CQDs electrocatalyst; (I) Faraday efficiency at different potential of Cu-SACs N CQDs; (J, K) HAADF-STEM image of all the Cu species on the carbon-dots Cu-N-CQDs (scale bar: 2nm). (Reproduced with permission[103]. Copyright 2024, Elsevier B.V.). HAADF-STEM: High-angle annular dark-field scanning transmission electron microscopy; FE: Faraday efficiency; SACs: Single-atom catalysts; TEM: Transmission electron microscope; CQDs: Carbon quantum dots.

reaction at 160 °C in the presence of citric acid for six h[103]. Figure 8H-K displays the structural schematic diagram and high-angle annular dark-field scanning transmission electron microscopy (HAADF-STEM) image of the Cu SAC N-CQD. The selectivity of CH_3CH_2OH is highly related to the coordination of Cu SACs, and changes with the variation of Cu loading. During the CO_2 reduction progress, the *in-situ* generated Cu is the active site, which is beneficial for the production of CH_3CH_2OH. This catalyst had a unique Cu-N-C site and achieved an FE of 70% for CH_3CH_2OH at -0.2 V *vs.* RHE [Figure 8I], as well as a stability exceeding 50 h. Pan *et al.* designed C-supported Cu catalysts with atomic-dispersed N, OH-Cu_3 sites Cu-N/interconnected mesoporous carbon fiber (IPCF)[104]. Atomically dispersed and N-coordinated Cu moieties were loaded onto a mesoporous N-doped carbon fiber carrier. The N, OH-Cu_3 sites had moderate *CO adsorption affinity and low barrier for *CO hydrogenation. Cu-N/IPCF could enhance nano confinement to prevent CO from escaping mesochannels, which greatly increased the residence time of *CO, and continuously reduced to CH_4 on Cu sites. At 300 mA cm^{-2}, this catalyst showed a high FE of CH_4 of 74.2%.

The coordination of Cu single atoms with N to form Cu-N_x sites results in various CO_2RR products during electroreduction. Dong *et al.* synthesized locally planar, symmetrically fractured planar-symmetry-broken CuN_3 (PSB-CuN_3) SACs[92]. The catalyst exhibited an FE of HCOOH of 94.3% at -0.73 V *vs.* RHE and could run stably in a flow cell for 100 h. The active centers of formate products were highly concentrated in the CuN_3 region. In the CO_2RR process, CuN_4C_4 sites tended to produce *COO-, while CuN_3C_3 and CuN_2C_2 tended to produce *CHO. Compared with highly symmetrical CuN_4C_4, the ΔG (0.23 eV) of the HCOOH on CuN_3C_3 was much lower than that of CO (0.68 eV), CH_4/CH_3OH (0.78 eV), and HER (1.01 eV). Xia *et al.* prepared ultra-high density Cu single atoms on thin-walled N-doped carbon nanotubes (TWN)[105], named TWN-$Cu_{13.35}$-600-SACs, with a Cu content of 13.35 wt%. The researchers established that the adjacent Cu-N_3 site was the active site. The FE of CH_3CH_2OH improved with the increase of the density of Cu-N_3 sites. As shown in Figure 9A-C, in H-cell, the highest FE of CH_3CH_2OH was about 81.9%. In addition, the stability of the catalyst exceeded 25 h. Xu *et al.* synthesized a Cu SAC (Cu-N_4-NG) based on N-doped graphene (NG) using a two-step pyrolysis method[106]. Cu atoms coordinated with four adjacent N atoms. They found that Cu-N_4 portion was beneficial for the CO_2 activation step. The CO_2RR on Cu-N_4-NG was less thermodynamically hindered, effectively limiting HER. Cu-N_4-NG achieved an FE of CO of 80.6% at -1.0 V *vs.* RHE. Cheng *et al.* prepared Cu-N_4-C/1100 containing Cu-N_4[107]. They adjusted the coordination environment and electronic structure of Cu through pyrolysis. The edge-hosted Cu-N_4 was the key active site for generation CO, which strongly interacted with *COOH and facilitated the desorption of *CO. Compared with Cu-N_3-C/800, which contained Cu-N_3 sites, Cu-N_4-C/1100 exhibited excellent performance for CO production. At -0.9 V *vs.* RHE, the catalyst achieved an FE of CO of 98%. Karapinar *et al.* prepared Cu-N-C SACs using $CuCl_2$ as a Cu source through simple pyrolysis. Cu atoms were coordinated by four N atoms to form CuN_4 sites dispersed in an N-doped conductive carbon matrix[108]. During electrolysis, the separated sites instantaneously transformed into Cu NPs, which may be the active species. At -1.2 V *vs.* RHE, the FE of CH_3CH_2OH was 55%. As shown in Figure 9D and E, Zhao *et al.* encapsulated single-atom Cu on N-doped porous carbon (Cu-SA/NPC)[109]. They found that the reaction mainly occurred at the coordination sites between Cu and four pyrrole-N atoms (Cu-pyrrolic-N_4). The coordination of Cu with four pyrrole-N atoms reduced the free energies for CO_2 activation. Cu-SA/NPC could reduce CO_2 to CH_3COOH, CH_3CH_2OH, and CH_3COCH_3 products, and CH_3COCH_3 was the major product (FE = 36.7%). Generally speaking, Cu SACs with Cu-N_4 sites (CN = 4) have the best catalytic effect on CO_2RR and exhibit superior stability. Recently, Roy *et al.* used $CuCl_2$ solution as the Cu source to form Cu-N_2 sites by loading Cu single atoms onto a carbon nitride (CN) matrix through the metal ion exchange method [Figure 9F-H][110]. This catalyst had high-density (1.5 at%) single-atom sites. The cooperative Cu-Cu sites generated on the 9N pores in Cu-PTI synergistically enhanced the activity of the CO_2 to CH_4. As shown in Figure 9I and J, at -0.84 V *vs.* RHE, the FE of CH_4 was 68%.

Furthermore, Cu coordinated by heteroatoms can promote the formation of C_{2+} products. Wu *et al.* broke the coordination symmetry of Cu sites to form Cu-S_2N_1 sites in atomic precision in Cu_6 clusters [$Cu_6(MBD)_6$, MBD = 2-mercaptobenzimidazole][111], which was conducive to the generation of *COOH instead of *OCHO, thereby inducing the formation of more valuable hydrocarbons. At -1.4 V *vs.* RHE, the catalyst exhibited an FE of 65.5% for hydrocarbons, where FE of CH_4 and FE of C_2H_4 accounted for 42.5% and 23%, respectively. Recently, Lv *et al.* anchored Cu single atoms onto F, O, N-co-doped carbon composites (FONCDs) via precipitation reaction, and the prepared CuFONC catalyst had a stable CuN_2O_1 configuration and a high density of Cu SAs[112]. They established that the addition of F and O resulted in excellent stability of CuN_2O_1 during CO_2RR. The addition of F adjusted the 3*d* orbitals charge of Cu atom in CuFONC. The Cu coordinated with N/O atoms, and the Cu-N/Cu-O ratio was 2:1. The Cu-N site in CuFONC was found to be an adsorption site for *CO. At -1.3 V *vs.* RHE, FE C_2 was 80.5%.

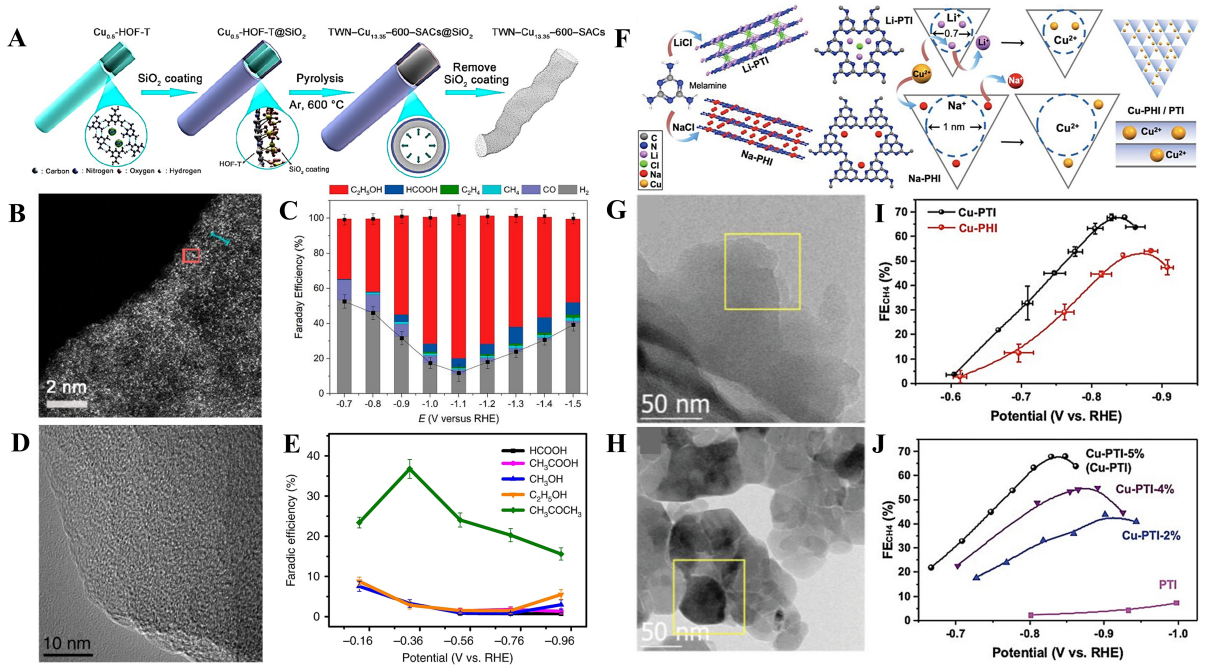

Figure 9. (A) Preparation and characterization of the catalysts; (B) HAADF-STEM images of TWN-$Cu_{13.35}$-600-SACs; (C) FE and the product distribution at different potentials. (Reproduced with permission[105]. Copyright 2023, American Chemical Society); (D) TEM images of Cu-SA/NPC. (E) FE of CO_2RR products on Cu-SA/NPC. [Reproduced with permission[109]. Copyright 2020, The Author(s)]; (F) Synthetic scheme of Na-PHI, Li-PTI; (G) HRTEM images of Na-PHI; (H) HRTEM images of Li-PTI; (I) FE of CH_4 comparison of Cu-PHI/PTI; (J) Partial current density of CH_4 for the catalysts. (Reproduced with permission[110]. Copyright 2024, Wiley-VCH GmbH). HAADF-STEM: High-angle annular dark-field scanning transmission electron microscopy; FE: Faraday efficiency; SACs: Single-atom catalysts; TWN: Thin-walled N-doped carbon nanotubes; Cu-SA/NPC: Single-atom Cu on N-doped porous carbon; CO_2RR: Carbon dioxide reduction reaction; TEM: Transmission electron microscope; PHI: Poly (heptazine imide); PTI: Poly (triazine imide); HRTEM: High-resolution transmission electron microscope.

The catalytic activity of Cu SACs is connected with the CN and degree of distortion of the Cu metal. Cu-N and Cu-C are effective active sites for CO_2RR. Cu-C and Cu-N sites generally generate hydrocarbons and oxygen-containing compounds, respectively. Researchers have found that a single Cu site usually produces C_1 products, and adjacent Cu can promote C-C coupling. It is difficult to precisely control the active sites, as they usually generate C_1 products, making it challenging to obtain C_{2+} products. Therefore, the key is to design the active site reasonably. Cu SACs with high CO_2RR performance can be designed by regulating the CN of Cu and N (Cu-N_4 being optimal), adjusting the loading density of Cu single atoms, and doping other heteroatoms to coordinate with Cu to saturate the Cu coordination sites.

CU-BASED CATALYST ADDITIVES

Cu has moderate *CO adsorption energy, which can form chemical bonds between adjacent CO molecules[113]. However, it is limited in the initial CO_2RR step (CO_2-CO), resulting in low CO surface coverage. A second metal component can be introduced to take advantage of its higher CO_2-CO reduction performance[114,115]. Au, Ag, Zn, and Ni have strong catalytic effects on the production of CO from CO_2RR. Additives can also adjust the acidity, alkalinity, and electronic structure of Cu-based electrocatalysts[116]. Regarding catalyst composition, the construction of two-component or multi-component catalysts has been shown to effectively improve CO_2RR efficiency[117,118] and simultaneously inhibit HER[119,120]. Combining Cu with other metals[113,121] usually exhibits in the characteristics of high selectivity, stable performance, and low overpotential[122,123].

CuAu

Ouyang *et al.* found that on Cu alloy catalysts such as CuAu and CuAg, the surface coupling hydrogenation activity was enhanced and indirectly inhibited solvent hydrogenation of intermediates, resulting in higher CH_3CH_2OH selectivity than Cu (100)[124]. Morales-Guio *et al.* deposited Au NPs by physical vapor deposition on top of polycrystalline Cu foil (Au/Cu)[125]. Au/Cu efficiently reduced CO_2 to CH_3CH_2OH. They observed that CO_2 was reduced to CO on Au NPs, which was then enriched and further reduced to alcohols on nearby Cu. Shen *et al.* synthesized AuCu alloy embedded in Cu submicron conical arrays (AuCu/Cu SCA)[114]. Cu atoms were replaced by larger Au atoms, causing lattice expansion and forming AuCu alloys. Altering the content of Au affected CO_2RR activity and the selectivity of C_2H_5OH/C_2H_4 products. The CO generated at Au sites coupled with $*CH_2$ intermediates at Cu sites to form $*COCH_2$, which further generated CH_3CH_2OH. In addition, the catalyst could maintain electrocatalytic activity for 24 h at high current densities. Wei *et al.* prepared an Au-doped Cu nanowire (Cu Au NWs)[126]. They modified a small amount of Au NPs on the surface of Cu NWs, using the homonuclear method. The addition of Au NPs resulted in a rougher surface, exposing more active sites. In addition, the *CO intermediates generated on Au NPs aggregate on Cu NWs, promoting the adsorption of *CO. The interface electrons transferred from Cu to Au induced electron-deficient Cu, which facilitates the adsorption of *CO. At -1.25 V *vs.* RHE, the FE C_{2+} increased from 39.7% of Cu NWs without Au to 65.3%. Zheng *et al.* successfully synthesized an Au-Cu Janus nanostructure catalyst (Au-Cu Janus NSs) using a seed growth strategy[127]. Cu atoms were deposited on one side of concave cubic Au seeds. The Au-Cu domain boundaries in the spatial separated Janus nanostructures facilitated synergistic catalysis. At -0.75 V *vs.* RHE, the FE C_{2+} was 67%.

CuAg

Ma *et al.* prepared Ag_{65}-Cu_{35} Janus nanostructure (JNS-100) catalysts with (100) facets [Figure 10A-C][128]. Compared to Cu, Ag_{65}-Cu_{35} JNS-100 had higher electron abundance. This catalyst exhibited the highest selectivity for C_2H_4 and C_{2+} products with FE values of 54% and 72%, respectively [Figure 10D-F]. As mentioned earlier, Cu (100) had a lower energy barrier for C-C coupling[49]. As shown in Figure 10G, Ag_{65}-Cu_{35} JNS-100 exposed Cu (100), Janus nanostructure induced tandem catalysis and electron transfer between Ag and Cu. Wei *et al.* improved the FE C_{2+} in CO_2RR by concatenating nano electrocatalysts[129]. As shown in Figure 10H, they designed a three-dimensional (3D) catalyst electrode with Ag NPs, which were deposited at the bottom of a Cu nanoneedle array (Cu needle-Ag) to generate the intermediate product CO. The dense Cu needles would prevent CO from flowing out of the Ag NPs, causing further dimerization of CO on the Cu nanoneedles to form C_{2+} products. Through this nanostructure design, FE C_{2+} was 70% in a flow cell. Choi *et al.* synthesized a tight atomic Cu-Ag interface on the Cu NW surface[130]. The tight atomic Cu-Ag interface promoted the synergistic effect of CO-Ag* and H-Cu*, greatly improving the selectivity of CH_4. The maximum FE of CH_4 at -1.17 V *vs.* RHE was 72%. Hoang *et al.* electrodeposited 3,5-diamino-1,2,4-triazole inhibitors on thin CuAg alloy films[123]. The CO_2RR performance of the alloy wire with an Ag content of 6% was the best, achieving an FE of nearly 60% and 25% for C_2H_4 and C_2H_5OH, respectively, at low potentials of -0.7 V *vs.* RHE. CuAg wire (6%) exhibits Ag-Cu bonds. Also, the Ag-Ag distance in the CuAg film is slightly reduced, indicating that Ag atoms were at least partially alloyed with smaller Cu atoms. As shown in Figure 10I, Li *et al.* synthesized Ag,S-Cu_2O/Cu catalysts through an *in-situ* dual doping strategy[131]. This catalyst had a typical 3D porous architecture which resulted in more active sites. The Cu atoms near heteroatoms in Cu_2O/Cu served as efficient active centers for CH_3OH production. S^- could regulate the electronic structure and morphology, while Ag^+ inhibited HER. FE of CH_3OH reached 67.4%. Du *et al.* cascaded Ag NPs and AgCu single-atom alloy (SAA) (AgCu SANP)[132]. The Ag NPs selectively reduced CO_2 to CO, followed by the formation of multiple carbon products on AgCu SAA. Owing to the asymmetric binding of Cu atom to the adjacent Ag atom, the incorporation of the single Ag atom enhanced the adsorption energy of CO on the Cu sites. At -0.65 V *vs.* RHE, FE C_{2+} reached 94% ± 4% under a working current density of about 720 mA cm^{-2}. Qi *et al.* synthesized CuAg alloy catalysts (CO_2-10-$Cu_{94}Ag_6$) by the

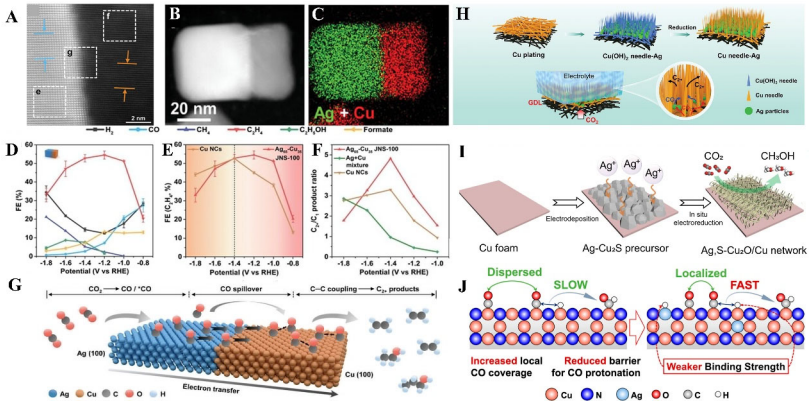

Figure 10. (A) HAADF-STEM image of Ag/Cu interface in Ag_{65}-Cu_{35} JNS-100; (B) HAADF-STEM images of Ag_{65}-Cu_{35} JNS-100; (C) EDS elemental mappings of Ag_{65}-Cu_{35} JNS-100; (D) FE of major CO_2-reduction products obtained on Ag_{65}-Cu_{35} JNS-100; (E) Comparison of C_2H_4 FE between Ag_{65}-Cu_{35} JNS-100 and Cu NCs at different potentials; (F) Comparison of C_{2+}/C_1 product ratios between Ag_{65}-Cu_{35} JNS-100, Ag + Cu mixture and Cu NCs; (G) Schematic illustration of a plausible CO_2RR mechanism on Ag_{65}-Cu_{35} JNS-100. (Reproduced with permission[128]. Copyright 2022, Wiley-VCH GmbH); (H) Schematic illustration of the synthesis of Cu needle-Ag catalyst. (Reproduced with permission[129]. Copyright 2023, Advanced Functional Materials published by Wiley-VCH GmbH); (I) Schematic diagram of the *in situ* dual-doping process for preparing the x, y-Cu_2O/Cu catalysts. [Reproduced with permission[131]. Copyright 2022, The Author(s)]; (J) Introduction of Ag into Cu_3N with weaker binding strength with reaction intermediates of CO_2RR could increase local CO coverage and facilitate *CO protonation to *CHO. (Reproduced with permission[134]. Copyright 2024, American Chemical Society). HAADF-STEM: High-angle annular dark-field scanning transmission electron microscopy; JNS: Janus nanostructure; FE: Faraday efficiency; NCs: Nanocrystals; CO_2RR: Carbon dioxide reduction reaction; EDS: Energy dispersive spectrometer.

co-electrodeposition method[133]. Under CO_2-supersaturated conditions, the co-deposition of Ag and Cu forms a CuAg alloy, with the Cu (100) facets being preferentially exposed. The dispersed Ag atoms on Cu strengthened C-O bond of C_3 chain. The FE 2-propanol in the H-cell with 1.0 mol L^{-1} $CsHCO_3$ was 56.7%. They observed that C_3 products can only be detected when the electrolyte cation is Cs^+ and CO_2 is supersaturated. This was attributed to the larger radius of Cs^+ that can interact with two *CO. Recently, Li *et al.* synthesized Cu_3N-Ag NCs by doping Ag into Cu_3N nanocubes (NCs)[134]. The Ag sites generated CO, while the Cu sites promoted C-C coupling to *COCHO, which enhanced the production of C_2H_4. As shown in Figure 10J, the cascade Ag-Cu dual sites in Cu_3N-Ag NCs could promote C-C coupling and generate C_2H_4.

CuZn

In 2017, Kattel *et al.* established that the ZnO/Cu (111) interface sites were the real active sites of CuZn catalysts that could reduce CO_2 to CH_3OH[135]. The synergistic effect of Cu and ZnO facilitated the synthesis of CH_3OH. Zhu *et al.* prepared Cu/ZnO-CeO_2 catalysts by the flame spray pyrolysis method[136], and the catalysts exhibited better CH_3OH selectivity (70%) than Cu/ZnO and Cu/CeO_2. In 2022, Amann *et al.* found that the hydrogenation of CO_2 preferentially occurred on ZnO[137]. Wan *et al.* found that phase-separated bimetallic Cu-Zn catalysts had a lower energy barrier to form the *COOH than the core-shell one[138]. The FE of CO was 94% and stability exceeded 15 h. Zhen *et al.* found that the synergistic effect between Cu and Zn can result in effective CO adsorption. Both balanced Cu-Zn sites and Zn-rich Cu-Zn sites promoted C-C coupling[139]. Recently, as shown in Figure 11A-D, Zhang *et al.* developed CuZn alloy/CuZn aluminate oxide (Al_2O_4) composite electrocatalyst ($Cu_9Zn_1/Cu_{0.8}Zn_{0.2}Al_2O_4$)[140]. The Al_2O_4 triggered a robust electron interaction among Cu, Zn, and Al, leading to the generation of numerous highly reactive interfaces characterized by exceptional activity. Supported by interface effects, the optimized catalyst achieved an FE C_{2+} of 88.5% and a current density of up to 400 mA cm^{-2} [Figure 11E-J].

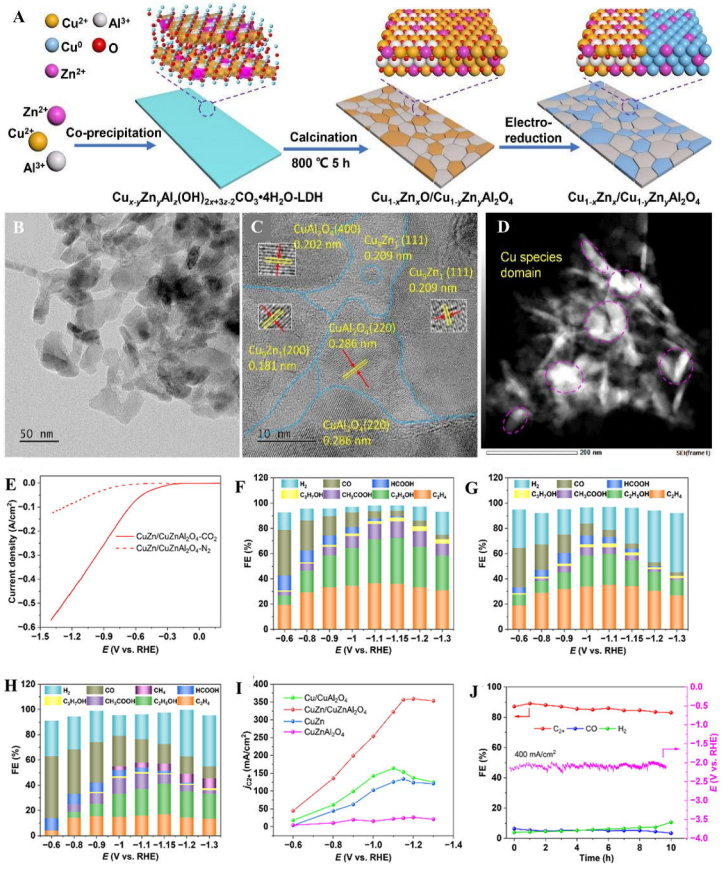

Figure 11. (A) Schematic illustration for the preparation of the CuZn/$CuZnAl_2O_4$ catalyst; (B) TEM image; (C) HR-TEM image; (D) HAADF-STEM image; (E) LSV curves toward CO_2RR on CuZn/$CuZnAl_2O_4$; Product distributions and corresponding FE produced by CuZn/$CuZnAl_2O_4$ (F); Cu/$CuAl_2O_4$ (G); and CuZn (H); (I) C_{2+} partial current density; (J) Stability test of CuZn/$CuZnAl_2O_4$. (Reproduced with permission[140]. Copyright 2023, ELSEVIER B.V. and Science Press). HAADF-STEM: High-angle annular dark-field scanning transmission electron microscopy; CO_2RR: Carbon dioxide reduction reaction; TEM: Transmission electron microscope; HR-TEM: High-resolution transmission electron microscope; LSV: Linear sweep voltammetry.

Others

Liu *et al.* loaded Ni SAC onto Cu catalyst using the electrostatic self-assembly method[141]. This catalyst promoted the dimerization of CO, reaching an FE of C_2H_4 of approximately 62% at -1.4 V *vs.* RHE. At 500 mA cm^{-2}, the catalyst could sustain stability for 14 h. Recently, Song *et al.* prepared a double-layer hollow spherical nanosphere catalyst (Ni-SA@Cu-NP)[142]. The inner layer of Ni-SA@Cu-NP was composed of dispersed Ni atoms, and the outer carbon layer consisted of Cu NPs. CO was generated on the Ni site in the inner layer, accumulated in the cavity, and then overflew to the outer Cu site for CO dimerization, achieving FE C_{2+} of 74.4%. The addition of In often reduced CO_2 to HCOOH. Wei *et al.* prepared a series of bimetallic In_xCu_y NP electrocatalysts[143]. They adjusted the growth direction of the crystal face by changing the molar ratio of In/Cu. Among the catalysts, $In_{1.5}Cu_{0.5}$ NPs had an FE of HCOOH of 90% at -1.2 V *vs.* RHE. Wang *et al.* prepared an In_2O_3/Cu catalyst with 3D succulent plant morphology[144]. The surface tensile strain and interfacial electronic interaction reduced the energy barrier for the formation of *HCOO. At -1.4 V *vs.* RHE, FE of HCOOH was 87.5%. Li *et al.* prepared a metal Cu/Pd-1% catalyst[145]. The Pd element was uniformly distributed on the Cu NPs. The doping of Pd revealed the *d*-band center of Cu toward the Fermi level. The higher *d*-band center location favors the adsorption of intermediates. This catalyst enhanced the affinity for *CO, exhibiting an FE C_{2+} of 66.2%. Zheng *et al.* introduced a single-atom Pb alloy Cu catalyst (Pb_1Cu) [Figure 12A and B][146], which could completely convert CO_2 to HCOOH with an FE of nearly 96%.

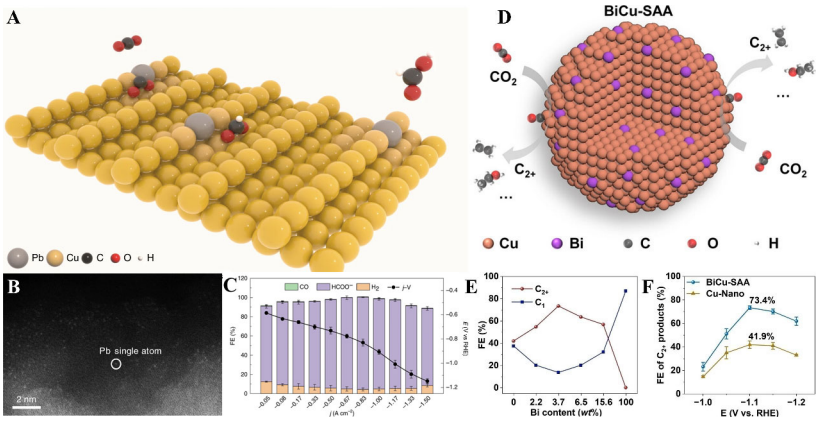

Figure 12. (A) Schematic illustration of CO_2 conversion into HCOOH over a Pb_1Cu SAA; (B) HAADF-STEM image and (C) FEs of all reduction products and *j-V* curves of Pb_1Cu catalyst. [Reproduced with permission[146]. Copyright 2021, The Author(s), under exclusive license to Springer Nature Limited]; (D) Schematic diagram of BiCu-SAA (E) The FEs of CO_2RR products on the catalysts with different Bi content at an applied potential of -1.10 V; (F) FE of C_{2+} products on the BiCu-SAA and control Cu-Nano catalysts at different applied potentials. (Reproduced with permission[147]. Copyright 2023, Wiley-VCH GmbH). HAADF-STEM: High-angle annular dark-field scanning transmission electron microscopy; CO_2RR: Carbon dioxide reduction reaction; FE: Faraday efficiency; SAA: Single-atom alloy.

The activation of Cu sites on Pb_1Cu catalyst directed CO_2RR towards the HCOO* instead of the COOH*. As shown in Figure 12C, the highest FE of HCOOH was 95.7% at -0.72 V *vs.* RHE, and an FE exceeding 80% could still be maintained even when the partial current density was up to -1200 mA cm^{-2}. Yang *et al.* prepared rod-like bimetallic $CuBi_{75}$ catalysts[122]. Bi, C, and O were uniformly dispersed on $CuBi_{75}$ catalysts. At -0.77 V *vs.* RHE, FE of HCOOH was 100%. As shown in Figure 12D, Cao *et al.* introduced single Bi atoms on Cu NPs to form BiCu-SAA[147]. The single-atom Bi on the Cu (111) surface resulted in significant charge redistribution. Local electrons can be transferred to the antibonding orbitals of CO_2 molecules, thereby activating and further reducing CO_2. As shown in Figure 12E and F, the FE C_{2+} of the BiCu-SAA catalyst was 73.4%, and the catalyst remained stable at the current density of 400 mA cm^{-2}.

Hu *et al.* synthesized $La(OH)_3$/Cu by modifying the Cu catalyst with $La(OH)_3$[148]. The modification of $La(OH)_3$ caused Cu to be in an electron-deficient state, which favored *CO adsorption and *CO-*COH coupling, thus increasing C_{2+} selectivity. The main component was C_2H_4. This catalyst achieved an FE C_{2+} of 71.2%, which was 1.2 times higher than that of pure Cu, and exhibited a current density of up to 1,000 mA cm^{-2}. Li *et al.* doped the *p*-block metal atom Ga into Cu and prepared a CuGa catalyst[149]. At -1.07 V *vs.* RHE, the CuGa catalyst exhibited an excellent FE C_{2+} of 81.5% at a current density of 0.9 A cm^{-2}. When the current density reached 1100 mA cm^{-2}, the catalyst still maintained a high FE C_{2+} of 76.9%. It was attributed to the p-d hybrid interaction between Ga and Cu, which redistributed the electronic structure and improved the bonding strength of intermediates. This finesse can also be expanded to other p-block metals, such as Al and Ge. Xie *et al.* synthesized a bimetallic Mg-Cu catalyst[150]. The modification with Mg not only enhanced the activation of CO_2 but also stabilized the Cu sites. Compared to Cu catalysts, Mg-Cu catalysts had abundant Cu^+ sites and stronger adsorption capacity for CO_2 and CO. The FE C_{2+} of the catalyst reached 80% (mainly C_2H_4), and the current density reached 1 A cm^{-2}.

Generally speaking, introducing other metals as additives can effectively improve CO_2 reduction efficiency. The metals used for doping and the levels of doping significantly influence both the products and the efficiency. For instance, introducing hydrophilic metals may result in the preferential formation of oxygen-containing compounds. The interaction between two metals usually improves CO_2 reduction efficiency and leads to high selectivity for C_{2+} products. When Cu forms an alloy with other metals, the

diversity in electronegativity can lead to charge transfer, resulting in a change in the *d*-band center of active sites. This electronic effect can regulate the adsorption of key intermediates. The addition of various metals often leads to different products. The Cu-Au catalysts are often beneficial to the production of CH_3CH_2OH. The Cu-Ag catalysts usually facilitate the generation of oxygen-containing C_{2+} products. The Cu-Zn catalysts are favorable to the production of C_2H_4. The addition of In, Bi and Sn usually leads to HCOOH. At the same time, doping with other metals can also achieve high current densities, some of which can reach industrial-grade current densities, and there is hope for commercialization. However, most of the doped metals are precious metals, and their use is not very economical. Furthermore, strong interactions between alloy components can lead to better catalytic performance of alloy catalysts than single-component NPs[151,152].

CU-BASED CATALYST SUPPORTS

When preparing Cu-based catalysts, it is necessary to load Cu NPs or Cu SAs on conductive materials to enhance catalytic activity. Choosing a suitable carrier can stabilize and enhance the electrocatalytic effect of these catalysts[9]. Common carriers include C-based materials (such as CB[153], carbon nanotubes, and graphene), N-doped carbon (NC) materials, and oxide carriers[154,155]. There are also some other types of carriers, such as MXene and metal-organic frameworks (MOFs).

C-based materials

C-based materials are commonly used to disperse SACs due to their advantages such as low cost, good stability, and good conductivity[156]. The properties of the substrate can change the electronic state of the active sites, thereby altering the reaction pathway and catalytic mechanism. To prepare commercial carbon-supported Cu SACs, Xu *et al.* mixed bulk Cu with molten Li and subsequently added CB as the support (Vulcan XC-72), followed by leaching LiOH by thoroughly mixing with water, in which process Cu atoms transferred to the carbon surface[153]. On this support, Cu single atoms can be highly dispersed. Cu was still atomically dispersed after prolonged electrocatalysis. At -0.7 V *vs.* RHE, FE of CH_3CH_2OH achieved 91%. The stability exceeded 16 h. Recently, Pan *et al.* developed a dual continuous mesoporous carbon carrier (IPCF) to support the synthesis of Cu-N/IPCF catalysts from Cu single atoms[104]. They designed carbon supported Cu catalysts by regulating the atomic scale structure of Cu active sites and designing the mesoscale structure of carbon supports. The catalyst was derived from block copolymers and had interconnected mesopores. Its unique long-range channel provided a microenvironment lacking H_2O, prolonging the transport pathway of CO intermediates. And this catalyst had N, OH-Cu_3 sites, which effectively inhibited HER and achieved an FE of CH_4 of 74.2% at 300 mA cm^{-2}. As shown in Figure 13A-C, Yang *et al.* prepared a through-hole carbon nanofiber catalyst with a large and uniformly distributed Cu single-atom modification CuSAs/through-hole carbon nanofibers (TCNFs)[157]. Due to the self-supporting and through-hole structure of the catalyst, a large number of Cu SAs were fully exposed on the surface, which was conducive to capturing CO_2. At -0.9 V *vs.* RHE, FE of CH_3OH was 44%, and the CH_3OH partial current density was -93 mA cm^{-2}.

NC materials

NC materials are ideal carriers due to their tunable pore structure, intense metal-heteroatom interactions, and stability[104,158]. Compared with C-based materials, NC materials contain N species, a higher N content, and a uniform N arrangement, which can provide abundant and more accurate coordination sites for single atoms[159]. Feng *et al.* used B- and N-doped graphene materials (N-doped GDY and B-doped GDY) as supports to anchor individual Cu atoms[160]. They found that Cu@doped GDY can spontaneously capture CO_2. Cu atoms had strong interactions with adjacent C, B, or N atoms. The electronegativity of coordinated elements is a crucial factor in improving catalytic performance. They discovered that the catalytic performance of Cu@N-doped GDY was better. Recently, as shown in Figure 13D-G, Xu *et al.* prepared

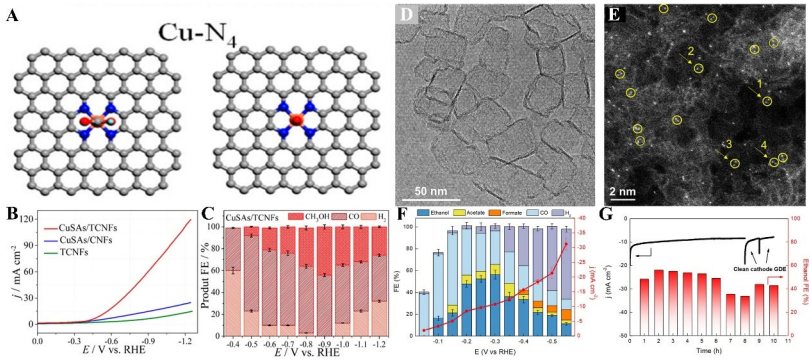

Figure 13. (A) Pyridine Cu-N_4 structure; (B) LSV curves and (C) FE of all products at CuSAs/TCNFs. (Reproduced with permission[157]. Copyright 2019, American Chemical Society); (D) TEM image and (E) corresponding enlargement of the sites 1-4 and intensity profiles of Cu_1/hNCNC; (F) FE, current density (*j*), and product distribution for Cu_1/hNCNC at different polarization potentials; (G) Ethanol FE and j as a function of time for Cu_1/hNCNC during a chronoamperometric test at -0.30 V. (Reproduced with permission[161]. Copyright 2024, American Chemical Society). FE: Faraday efficiency; LSV: Linear sweep voltammetry; CuSAs/TCNFs: Cu Single Atoms/through-hole carbon nanofibers; TEM: Transmission electron microscope; hNCNCs: NC nanocages.

Cu_1/hNCNC by vapor deposition on multi-stage NC nanocages (hNCNCs) using commercial Cu_2O powder as a Cu source[161]. This catalyst had CuOCu-N_4-oxygen-bridged binuclear Cu sites on hNCNCs. Cu_1/hNCNC exhibited the most advanced low overpotential for C_2H_5OH at 0.19 V *vs.* RHE, with FE of CH_3CH_2OH reaching 56.3% at -0.30 V *vs.* RHE, and the Cu active site was very steady during the CO_2RR process.

Cu NPs usually employ C-based materials and oxides as supports, and the interaction between appropriate supports and Cu NPs can improve the selectivity of the product[156]. For example, the *g*-C_3N_4 supports can not only elevate the *d*-orbital of Cu to the Fermi level, but also serve as an additional active center for CO_2RR, enhancing the selectivity of CH_4 and C_2H_4[162]. As shown in Figure 14A and B, Li *et al.* synthesized CuNCN by the precipitation method, using CuCl as a Cu source and adding $NH_3•H_2O$ and cyanamide (H_2NCN), and then prepared Cu-based/C_xN_y catalysts by pyrolysis of CuNCN[163]. The state of Cu species on the g-C_3N_4 carrier was regulated by the pyrolysis temperature. Among the prepared catalysts, CuNCN-300 obtained by pyrolysis of CuNCN at 300 °C had the highest FE of C_2H_4 of 48.5% and a current density of 500 mA cm^{-2}. The good dispersibility of Cu_3N in CuNCN-300 promoted the selectivity of C_2H_4, while the tris-*s*-triazine structure (*g*-C_3N_4 fragment) in C_xN_y enhanced the reaction of *CO - *CHO on the Cu surface. Li *et al.* prepared a *p*-NG-Cu-7 catalyst by loading 7-nm Cu NPs on pyridine-rich N-graphene (*p*-NG)[164]. As shown in Figure 14C, due to the rich Lewis base sites of *p*-NG, the formation of *COOH was promoted, which was then enriched on Cu NPs and converted into CO and CH_xO with subsequent C-C coupling. Compared with the catalytic performance of GO-Cu-7 catalyst deposited on conventional graphene (FE of C_2H_4 = 7.5%), the *p*-NG-Cu-7 catalyst had an FE of C_2H_4 of 19%, and the selectivity of C_2H_4 in hydrocarbons reached 79%. The *p*-NG-Cu-7 catalyst could also produce C_2H_5OH with 63% FE.

Oxides

The synergistic effect between metal oxide carriers and Cu can modulate the electronic structure of the catalyst. Loading Cu on oxide (ZnO/Al_2O_3) can promote the reduction of CO_2 to CH_3OH[165]. The Lewis acid sites in metal oxides (such as Al_2O_3 and Cr_2O_3) have been proven to activate CO_2 molecules and promote CO_2 methanation[166-169]. As shown in Figure 15 A, Chen *et al.* anchored Cu SAs to ultra-thin porous Al_2O_3 rich in Lewis acid centers (Cu/Al_2O_3 SAC)[170]. When Cu single atoms were supported by ultra-thin porous Al_2O_3, the Cu/Al_2O_3 SAC achieved an FE of C_2H_4 of 62%. As shown in Figure 15B and C, Cu atoms on Al_2O_3 were in a higher oxidation state (electrons transferred from Cu atoms to the carrier). In addition, the Cu

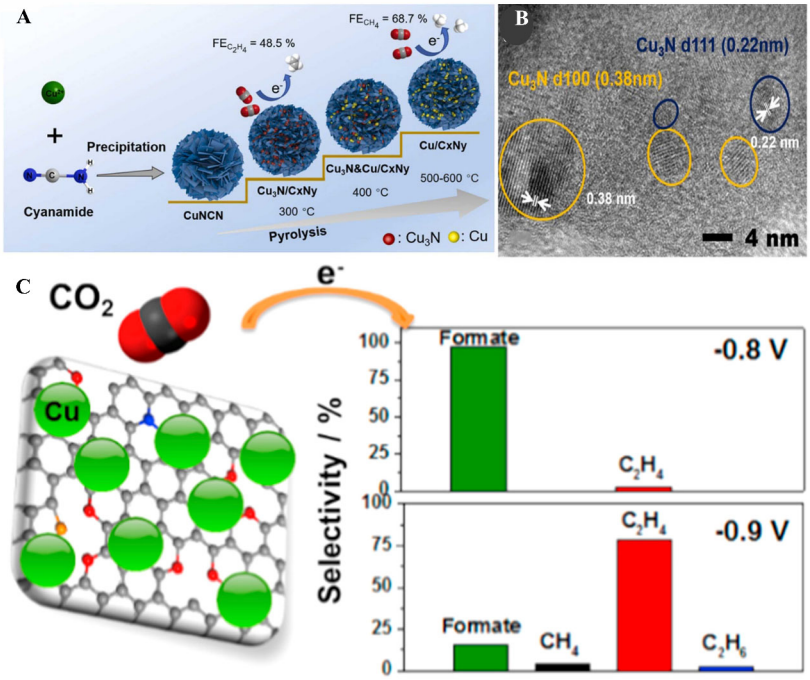

Figure 14. (A) The schematic illustration of synthesis of CuNCN and preparation of Cu-based/C_xN_y by CuNCN pyrolysis; (B) HRTEM of CuNCN-300. (Reproduced with permission[163]. Copyright 2022, Elsevier B.V. All rights reserved); (C) Product selectivity of the hydrocarbons generated from the *p*-NG-Cu-7 catalyzed reduction at -0.9 V. (Reproduced with permission[164]. Copyright 2016, Elsevier Ltd). NCN: Elements N and C; HRTEM: High-resolution transmission electron microscope.

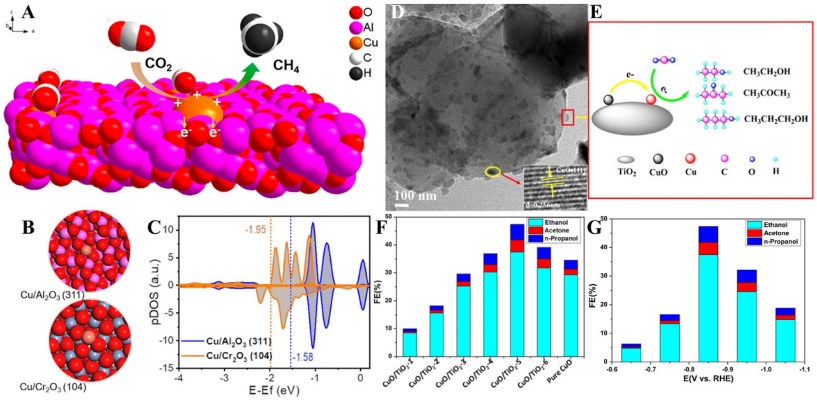

Figure 15. (A) Schematic diagram of CO_2RR on Cu/Al_2O_3 SAC; (B) Electronic structure and (C) projected densities of states (pDOS) of *d*-orbitals with an aligned Fermi level of Cu/Al_2O_3 SAC and Cu/Cr_2O_3 SAC. Color code: Cu, brick red; Al, purple; Cr, gray; O, red. (Reproduced with permission[170]. Copyright 2021, American Chemical Society); (D) TEM images of CuO/TiO_2-5 catalyst in low magnification; (E) Schematic diagram of CO_2RR on CuO/TiO_2-5 catalyst; (F) FEs for different products over various CuO/TiO_2 catalysts at -0.85 V *vs.* RHE in CO_2-saturated 0.5 M $KHCO_3$ aqueous solution; (G) FEs for different products over CuO/TiO_2-5 catalyst at various potentials. (Reproduced with permission[171]. Copyright 2018, MDPI, Basel, Switzerland). CO_2RR: Carbon dioxide reduction reaction; SAC: Single-atom catalysts; FE: Faraday efficiency; RHE: Reversible hydrogen electrodes; TEM: Transmission electron microscope.

atoms on Al_2O_3 exhibited higher *d*-band centers, indicating an improved electron transfer ability. The electron-accepting properties of Al_2O_3 were beneficial for stabilizing methanation intermediates and reducing the energy barrier. TiO_2 could stabilize Cu NPs and provide more active sites. As shown in Figure 15D and E, Yuan *et al.* prepared CuO/TiO_2 catalysts by the hydrothermal method using CuO and TiO_2 and then reduced them *in situ* to Cu/TiO_2 catalysts[171]. TiO_2, as a semiconductor material, can serve as

an oxidation-reduction electron carrier and assist in CO_2 adsorption[172-174]. It can stabilize the CO_2RR intermediates and reduce overpotential. The CuO/TiO_2 significantly increased the adsorption capacity of CO_2. Firstly, a large amount of CO_2 was adsorbed on TiO_2. Then, the adsorbed CO_2 obtained an electron from the Cu/TiO_2 and was converted to CO_2^-, which could be dimerized to $^*C_2O_2^-$. As shown in Figure 15F and G, the Cu/TiO_2 catalyst effectively reduced CO_2 to multiple oxygen-containing carbon compounds such as CH_3CH_2OH, CH_3COCH_3, and $CH_3CH_2CH_2OH$. The maximum total FE was 47.4%.

Others

Abdinejad *et al.* synthesized Cu-Pd/MXene catalysts using MXene-based ($Ti_3C_2T_x$) materials as carriers[175]. They paired 2D MXene with bimetallic Cu-Pd. Compared with Cu-Pd, the Cu-Pd/MXene had a larger active surface area and electron transfer rate. This stemmed from MXene improving electron transfer and having a larger electrochemically active surface area (EASA). Due to the unique multi-layer composition of MXene, the catalytic surface area and conductivity increased. At -0.5 V *vs.* RHE, FE of HCOOH reached 93%, and overall battery energy efficiency (EE) reached 47%. MOFs are considered as the ideal catalyst supports. The Cu-N coordination bond formed by Cu(II) and N-heterocyclic ligands has moderate strength, located between Cu-O coordination and Cu porphyrin bond[176]. Thus, Cu-N coordination is more stable. Therefore, Chen *et al.* designed a MOF (2Bn-Cu@UiO-67) of encapsulated N-heterocyclic carbene (NHC) ligand linked to Cu SAC[177], which exhibited an FE of CH_4 of 81%. Due to the interaction between Cu and NHCs, the electron occupancy rate on the *d* orbital was much lower than that of Cu foil. The σ donation from NHC enriched the electron density of Cu single atoms, promoting the adsorption of CHO*. The high porosity promoted the spread of CO_2 molecules towards 2Bn-Cu, remarkably improving the catalytic efficiency.

The above results indicate that the appropriate carrier can improve the performance and selectivity of the catalyst, and some supports can enhance catalyst stability.

The following Table 2 lists the catalytic performance data of different types of Cu catalysts.

CONCLUSION AND OUTLOOK

In conclusion, with the development of catalyst synthesis and characterization methods, we gained a deeper comprehension of the catalytic CO_2RR process, the interaction mechanism with the reactants, and the dynamic evolution of the active sites. Cu NPs exhibit higher selectivity towards C_{2+} products. However, the C_{2+} products are often the sum of multiple products, and improving the selectivity of individual C_{2+} products remains crucial. The size and morphology of Cu NPs exert a considerable influence on the efficiency of CO_2RR, while the grain boundaries of Cu NPs affect the selectivity of CO_2RR products. Cu NPs with varying sizes and morphologies possess different crystal planes, which tend to generate different products. Surface modification of Cu NPs with different materials can increase CO_2RR activity. Cu SACs have a higher selectivity for single carbon products, especially CO and CH_4. The CO_2RR on Cu SACs is mainly influenced by the coordination environment and the support of Cu SACs. The selectivity and production efficiency of CO_2RR can be enhanced by precise regulation of the coordination environment. Cu SACs have a higher CO_2RR efficiency with N-coordination than with C-coordination and are the best coordinated by four N atoms, and the corresponding catalysts also exhibit the best stability. Especially the FE of CO products has reached nearly 100%. In terms of catalyst stability, the stability of Cu NPs is often inferior to that of Cu SACs. The possible reason is that coordination bonds can be formed between the support and single-atom Cu, thereby improving the stability of Cu SACs. Furthermore, adding additives and selecting appropriate carriers can also enhance catalytic performance and improve stability, providing ideas for designing Cu-based CO_2RR catalysts in the future.

Table 2. A summary of reported performance data for Cu-based CO_2RR electrocatalysts

Category	Catalyst	CO_2RR conditions	Potential/ V *vs.* RHE	FE	*j*/ mA cm^{-2}	Ref.
Cu NPs	7 nm n-Cu/C	0.1 M $NaHCO_3$, H-cell	-1.35	CH_4 = 76%	9.5	[60]
	20-nm Cu_2O NP/C	0.1 M $KHCO_3$, H-cell	-1.1	C_{2+} = 74%, C_2H_4 = 57.3%	27.5	[61]
	20 nm Cu NPs	5 M KOH, flow-cell	-0.73	C_{2+} = 70%	800	[63]
	Cu nanoneedles	3 M KCl, pH = 1, flow-cell	-2.3	C_{2+} = 90.69% ± 2.15%	1400	[64]
	o-Cu_2O with high-index facets	1 M KCl, H-cell	-1.1	C_{2+} = 48.3%	17.7	[65]
	F-Cu_2O with exposed (322) facets	0.1 M $KHCO_3$, H-cell	-1.2	C_2H_4 = 74.1%, for 12 h		[66]
	Cu_2O/Ppy with high refractive index (311) and (211) facets	0.5 M $KHCO_3$, H-cell	-0.85	CH_3OH = 93% ± 1.2%	0.223	[67]
	Cu_2O (CO) with abundant Cu (100) crystal planes	0.1 M $KHCO_3$, flow-cell	-1	C_{2+} = 77.4%, C_2H_4 = 56.6%	500	[68]
	P-Cu_2O-240	1 M KOH, flow-cell	-2.5	C_{2+} = 75.3% ± 3.1%	1000	[69]
	P-Cu	0.1 M $KHCO_3$, H-cell	-1.3	C_{2+} = 57.22%, C_2H_4 = 30%	40	[77]
	Cu-HoMSs	0.5 M $KHCO_3$, flow-cell	-0.88	C_{2+} = 77.0% ± 0.3%, (mainly C_2H_4 and CH_3CH_2OH)	513.7 ± 0.7	[79]
	Multihollow Cu_2O	2 M KOH, flow-cell	-0.61	C_{2+} = 75.2% ± 2.7%	342	[80]
	p-CuO-(12.5 nm)	3 M KOH, flow-cell	-0.87	C_2H_5OH = 44.1 ± 1%, C_{2+} = 90.6% ± 3.4%	501 ± 15	[78]
	fluorinated polymer-functionalized Cu-poly-1	1 M $KHCO_3$, flow-cell	-3.98	C_{2+} = 71.08%	500	[58]
	AN-Cu(OH)@Nafion	1 M KOH, flow-cell	-0.76	C_2H_4 = 44%	300	[52]
	Cu@Nafion-4	0.1 M $KHCO_3$, H-cell	-1.2	C_{2+} = 73.5%	13	[53]
	Cu-P1 with polyamines	10 M KOH, flow-cell	-0.47	C_2H_4 = 87% ± 3%		[81]
	Cu-12C	1 M KOH, flow-cell	-1.2	C_{2+} = 80.3%	321	[55]
	t-Cu_2O	0.5 M $KHCO_3$, H-cell	-1.1	C_2H_4 = 59%	22	[73]
	Cu (100)/Cu (111)	1 M $KHCO_3$, flow-cell	-0.6	C_{2+} = 74.9 ± 1.7%, for 50 h	300	[74]
	TA-Cu	1 M KOH, flow-cell	-0.7	C_2H_4 = 63.6%	497.2	[76]
	Cu SAs-GDY	0.1 M $KHCO_3$, flow-cell	-1.2	CH_4 = 81%, for 10 h	243	[99]
Cu SACs	Cu-SAs/HGDY	1 M KOH, flow-cell	-1.1	CH_4 = 44%	230.7	[98]
	Cu-CN	0.1 M $KHCO_3$, H-cell	-1.2	CH_4 = 49.04%	7.97	[100]
	Cu-N-C	0.5 M $KHCO_3$, H-cell	-0.67	CO = 98%	4.5	[101]
	Cu-CDs	0.5 M $KHCO_3$, H-cell	-1.44	CH_4 = 78%	40	[87]
	CuG-1000	1 M KOH, H-cell	-0.65	CO = 99%	6.53	[102]
	Cu SACs N-CQDs	0.1 M $KHCO_3$, H-cell	-0.2	CH_3CH_2OH = 70%, for 50 h	6.53	[103]
	Cu-N/IPCF	Alkaline electrolyte, flow-cell	-1.21	CH_4 = 74.2%	300	[104]
	PSB-CuN_3 SACs	0.5 M $KHCO_3$, flow-cell	-0.73	HCOOH = 94.3%, for 10 h	94.4	[92]
	TWN-Cu-600-SACs	0.5 M $CsHCO_3$, H-cell	-1.1	CH_3CH_2OH = 81.9%, for 25 h	35.6	[105]
	Cu-N_4-NG	0.1 M $KHCO_3$	-1	FE of CO = 80.6%		[106]
	Cu-N_4-C/1100	0.1 M $KHCO_3$, H-cell	-0.9	CO = 98%, for 40 h	3.3	[107]
	Cu-SA/NPC	0.1 M $KHCO_3$	-0.36	Acetone = 36.7%	7	[109]
	Cu-NC	1 M KOH, flow-cell	-0.84	CH_4 = 68%, for 12 h	348	[110]
	Cu/C-Al_2O_3 SAC	1 M KOH, flow-cell	-1.2	CH_4 = 62%	153	[170]
	CuSAs/TCNFs	0.1 M $KHCO_3$, flow-cell	-0.9	CH_3OH = 44%	93	[157]

	$Cu_6(MBD)_6$	1 M KOH, flow-cell	-1.4	CH_4 = 42.5%, C_2H_4 = 23%	183.4	[111]
	CuFONC	0.1 M $KHCO_3$, H-cell	-1.3	C_{2+} = 80.5%	60	[112]
	AuCu/Cu SCA	0.5 M $KHCO_3$, H-cell	-0.8	C_2H_4 = 16%, C_2H_5OH = 29%, for 24 h	4.9	[114]
Additive	Cu Au NWs	0.1 M $KHCO_3$ and 0.1 M KCl, H-cell	-1.25	C_{2+} = 65.3%, for 10 h	12.1	[126]
	Au-Cu Janus NSs	3 M KOH, flow-cell	-0.75	C_{2+} = 67%	290	[127]
	Cu needle-Ag	0.1 M $KHCO_3$, flow-cell	-1	C_{2+} = 70%	350	[129]
	Cu_9Ag_1NWs	0.1 M $KHCO_3$	-1.17	CH_4 = 72%		[130]
	CuAg-DAT	0.1 M $KHCO_3$, flow-cell	-0.7	C_2H_4 = 60%, C_2H_5OH = 25%	300	[123]
	Ag,S-Cu_2O/Cu	$BMImBF_4/H_2O$ = 1:3, flow-cell	-1.18	CH_3OH = 67.4%	122.7	[131]
	Ag_{65}-Cu_{35} JNS-100	0.1 M $KHCO_3$, H-cell	-1.4	C_2H_4 = 54%, C_{2+} = 72%	15.14	[128]
	AgCu SANP	1 M KOH, flow-cell	-0.65	C_{2+} = 94%	720	[132]
	$Cu_{94}Ag_6$	1 M $CsHCO_3$, H-cell	-0.73	2-propanol = 56.7%, for 24 h	59.3	[133]
	Cu_4Zn	0.1 M $KHCO_3$, H-cell	-1.05	CH_3CH_2OH = 29.1%	8.2	[11]
	Cu-Zn	0.1 M $KHCO_3$	-1	CO = 94%, for 15 h		[138]
	$Cu_9Zn_1/Cu_{0.8}Zn_{0.2}Al_2O_4$	2 M KOH, H-cell	-1.15	C_{2+} = 88.5%	25	[140]
	Ni SAC + Cu-R	1 M $KHCO_3$, flow-cell	-1.05 ~ -1.4	C_2H_4 = 62%, for 14 h	370	[141]
	Ni-SA@Cu-NP	1 M KOH, flow-cell	-1.2	C_{2+} = 74.4%, for 15 h	337.4	[142]
	$In_{1.5}Cu_{0.5}$NPs	0.1 M $KHCO_3$, H-cell	-1.2	HCOOH = 90%	3.59	[143]
	In_2O_3/Cu	0.5 M $KHCO_3$	-1.4	HCOOH = 87.5%		[144]
	Cu-In_2O_3	0.1 M $KHCO_3$, H-cell	-0.7	CO = 95%	3.7	[175]
	Cu/Pd-1%	1 M KOH, flow-cell	-1.8	C_{2+} = 66.2%	463.2	[145]
	Pb_1Cu	0.5 M $KHCO_3$, flow-cell	-0.72	HCOOH = 95.7%	500	[146]
	$CuBi_{75}$	0.5 M $KHCO_3$	-0.77	HCOOH = 100%		[122]
	BiCu-SAA	0.1 M $KHCO_3$, flow-cell	-1.1	C_{2+} = 74.3%, for 11 h	400	[147]
	$La(OH)_3$/Cu	0.1 M $KHCO_3$, flow-cell	-1.25	C_{2+} = 71.2%, for 8 h	1000	[148]
	CuGa	1 M KOH, flow-cell	-1.07	C_{2+} = 81.5%	900	[149]
	Mg-Cu	1 M KOH, flow-cell	-0.77	C_{2+} = 80%	1000	[150]

CO_2RR: Carbon dioxide reduction reaction; RHE: Reversible hydrogen electrode; NPs: Nanoparticles; HoMS: Hollow multi-shell structure; SACs: Single-atom catalysts; TWN: Thin-walled N-doped carbon nanotubes; PSB-CuN_3: Planar-symmetry-broken CuN_3; SCA: Submicron conical arrays; NWs: Nanowire; JNS: Janus nanostructure; SAA: Single-atom alloy; IPCF: Interconnected mesoporous carbon fiber; CQDs: Carbon quantum dots; DAT: 3,5-diamino-1,2,4-triazole inhibitors; SANP: single atoms and NPs alloy; FE: Faraday efficiency.

Cu-based catalysts are not stable enough, and future CO_2RR catalysts being able to precisely control the active sites to improve their comprehensive performance are the focus of research, mainly in the following areas:

Precise regulation of the coordination environment, electronic structure, and the unique interaction between the supports and the Cu sites of SACs is very important to achieve superior catalytic activities. For example, a second metal atom can be introduced to form dual-atom-site catalysts based on SACs while adjusting the type of coordination atoms and the spatial configuration to change the adsorption energy of Cu sites for CO_2 and adjust their catalytic performance.

NP-based single-atom sites, dual-atom sites, or clusters can be introduced to form nano-multiple-site catalysts and coexist with them. In this way, the respective advantages of these four species can be exploited in the same catalyst. The synergy in catalysis of different catalyst forms will be the future direction of CO_2RR since single-atom sites, dual-atom sites, clusters, and NPs have different roles in the reaction. In short, the process of CO_2RR is not singular. To obtain an efficient Cu-based catalyst, it is necessary to precisely control each catalyst component to perform its specific function, including components that enhance the adsorption energy of CO_2, components that reduce the reaction energy barrier, and components that efficiently remove reaction products.

The current density of Cu-based catalysts in CO_2RR is mostly low, and only a few can achieve industrial-grade current densities at high FE. Therefore, to achieve industrial commercialization, it is essential to identify appropriate strategies to increase the reaction current density. In addition to selectivity and current density, stability and one-way conversion efficiency are also crucial. It is necessary to study the dynamic changes on the surface of Cu-based catalysts and the evolution of active sites. Industrialization can be realized by developing industrial electrolytic cell devices.

DECLARATIONS

Authors' contributions

Contributed equally to this work: Li, Q.; Jiang, J.
Literature search and organization and manuscript drafting: Li, Q.; Jiang, J.
Provided administrative and software technical: Liu, D.; Xu, D.
Manuscript revision: Jiang, S.
Supervision and suggestion: Chen, Y.
Project supervision: Liu, X.; Zhu, D.

Availability of data and materials

Not applicable.

Financial support and sponsorship

The authors gratefully acknowledge the support of the National Natural Science Foundation of China (No. 22101150; No. 22101029; No. 52201261). This work was also supported by the Beijing Municipal Natural Science Foundation (2222006), the Scientific Research Program of BJAST (23CB020, 24CB003-11), and Beijing Municipal Financial Project BJAST Young Scholar Programs B (YS202202).

Conflicts of interest

All authors declared that there are no conflicts of interest.

Ethical approval and consent to participate

Not applicable.

Consent for publication

Not applicable.

REFERENCES

1. Ringe, S.; Clark, E. L.; Resasco, J.; et al. Understanding cation effects in electrochemical CO_2 reduction. *Energy. Environ. Sci.* **2019**, *12*, 3001-14. DOI
2. Kim, D.; Resasco, J.; Yu, Y.; Asiri, A. M.; Yang, P. Synergistic geometric and electronic effects for electrochemical reduction of carbon dioxide using gold-copper bimetallic nanoparticles. *Nat. Commun.* **2014**, *5*, 4948. DOI PubMed
3. Yang, D.; Zhu, Q.; Sun, X.; et al. Nanoporous Cu/Ni oxide composites: efficient catalysts for electrochemical reduction of CO_2 in aqueous electrolytes. *Green. Chem.* **2018**, *20*, 3705-10. DOI
4. Lu, L.; Zhong, H.; Wang, T.; Wu, J.; Jin, F.; Yoshioka, T. A new strategy for CO_2 utilization with waste plastics: conversion of hydrogen carbonate into formate using polyvinyl chloride in water. *Green. Chem.* **2020**, *22*, 352-8. DOI
5. Sun, H.; Xu, X.; Yan, Z.; et al. Superhydrophilic amorphous Co-B-P nanosheet electrocatalysts with Pt-like activity and durability for the hydrogen evolution reaction. *J. Mater. Chem. A.* **2018**, *6*, 22062-9. DOI
6. Wang, Y.; Han, P.; Lv, X.; Zhang, L.; Zheng, G. Defect and interface engineering for aqueous electrocatalytic CO_2 reduction. *Joule* **2018**, *2*, 2551-82. DOI
7. Zhang, H.; Wang, J.; Zhao, Z.; et al. The synthesis of atomic Fe embedded in bamboo-CNTs grown on graphene as a superior CO_2 electrocatalyst. *Green. Chem.* **2018**, *20*, 3521-9. DOI
8. Liu, M.; Pang, Y.; Zhang, B.; et al. Enhanced electrocatalytic CO_2 reduction via field-induced reagent concentration. *Nature* **2016**, *537*, 382-6. DOI
9. Xie, H.; Wang, T.; Liang, J.; Li, Q.; Sun, S. Cu-based nanocatalysts for electrochemical reduction of CO_2. *Nano. Today.* **2018**, *21*, 41-54. DOI
10. Woldu, A. R.; Huang, Z.; Zhao, P.; Hu, L.; Astruc, D. Electrochemical CO_2 reduction (CO_2RR) to multi-carbon products over copper-based catalysts. *Coord. Chem. Rev.* **2022**, *454*, 214340. DOI
11. Ren, D.; Ang, B. S.; Yeo, B. S. Tuning the selectivity of carbon dioxide electroreduction toward ethanol on oxide-derived Cu*x*Zn catalysts. *ACS. Catal.* **2016**, *6*, 8239-47. DOI
12. Kuhl, K. P.; Cave, E. R.; Abram, D. N.; Jaramillo, T. F. New insights into the electrochemical reduction of carbon dioxide on metallic copper surfaces. *Energy. Environ. Sci.* **2012**, *5*, 7050. DOI
13. Iijima, G.; Inomata, T.; Yamaguchi, H.; Ito, M.; Masuda, H. Role of a hydroxide layer on Cu electrodes in electrochemical CO_2 reduction. *ACS. Catal.* **2019**, *9*, 6305-19. DOI
14. Carroll T, Yang X, Gordon KJ, Fei L, Wu G. Ethylene electrosynthesis via selective CO_2 reduction: fundamental considerations, strategies, and challenges. *Adv. Energy. Mater.* **2024**, *14*, 2401558. DOI
15. Qin, Q.; Suo, H.; Chen, L.; et al. Emerging Cu-based tandem catalytic systems for CO_2 electroreduction to multi-carbon products. *Adv. Mater. Interfaces.* **2024**, *11*, 2301049. DOI
16. Zheng, W.; Yang, X.; Li, Z.; et al. Designs of tandem catalysts and cascade catalytic systems for CO_2 upgrading. *Angew. Chem. Int. Ed.* **2023**, *62*, e202307283. DOI
17. Chen, H.; Mo, P.; Zhu, J.; et al. Anionic coordination control in building Cu-based electrocatalytic materials for CO_2 reduction reaction. *Small* **2024**, *20*, e2400661. DOI
18. Machado AS, Nunes da Ponte M. CO_2 capture and electrochemical conversion. *Curr. Opin. Green. Sustain. Chem.* **2018**, *11*, 86-90. DOI
19. Li, L.; Li, X.; Sun, Y.; Xie, Y. Rational design of electrocatalytic carbon dioxide reduction for a zero-carbon network. *Chem. Soc. Rev.* **2022**, *51*, 1234-52. DOI
20. Hori, Y.; Kikuchi, K.; Suzuki, S. Production of CO and CH_4 in electrochemical reduction of CO_2 at metal electrodes in aqueous hydrogencarbonate solution. *Chem. Lett.* **1985**, *14*, 1695-8. DOI
21. Hori, Y.; Takahashi, R.; Yoshinami, Y.; Murata, A. Electrochemical reduction of CO at a copper electrode. *J. Phys. Chem. B.* **1997**, *101*, 7075-81. DOI
22. Murata, A.; Hori, Y. Product selectivity affected by cationic species in electrochemical reduction of CO_2 and CO at a Cu electrode. *Bull. Chem. Soc. Jpn.* **1991**, *64*, 123-7. DOI
23. Kortlever, R.; Shen, J.; Schouten, K. J.; Calle-Vallejo, F.; Koper, M. T. Catalysts and reaction pathways for the electrochemical reduction of carbon dioxide. *J. Phys. Chem. Lett.* **2015**, *6*, 4073-82. DOI PubMed
24. Zhang, L.; Zhao, Z. J.; Gong, J. Nanostructured materials for heterogeneous electrocatalytic CO_2 reduction and their related reaction mechanisms. *Angew. Chem. Int. Ed.* **2017**, *56*, 11326-53. DOI
25. Jones, J.; Prakash, G. K. S.; Olah, G. A. Electrochemical CO_2 reduction: recent advances and current trends. *Isr. J. Chem.* **2014**, *54*, 1451-66. DOI

26. Benson, E. E.; Kubiak, C. P.; Sathrum, A. J.; Smieja, J. M. Electrocatalytic and homogeneous approaches to conversion of CO_2 to liquid fuels. *Chem. Soc. Rev.* **2009**, *38*, 89-99. DOI PubMed
27. Hori, Y.; Murata, A.; Takahashi, R.; Suzuki, S. Electroreduction of carbon monoxide to methane and ethylene at a copper electrode in aqueous solutions at ambient temperature and pressure. *J. Am. Chem. Soc.* **1987**, *109*, 5022-3. DOI
28. Handoko, A. D.; Wei, F.; Jenndy; Yeo, B. S.; Seh, Z. W. Understanding heterogeneous electrocatalytic carbon dioxide reduction through operando techniques. *Nat. Catal.* **2018**, *1*, 922-34. DOI
29. Li, C.; Ji, Y.; Wang, Y.; et al. Applications of metal-organic frameworks and their derivatives in electrochemical CO_2 reduction. *Nanomicro. Lett.* **2023**, *15*, 113. DOI
30. Wang, K.; Liu, D.; Liu, L.; et al. Tuning the local electronic structure of oxygen vacancies over copper-doped zinc oxide for efficient CO_2 electroreduction. *eScience* **2022**, *2*, 518-28. DOI
31. Albo, J.; Vallejo, D.; Beobide, G.; Castillo, O.; Castaño, P.; Irabien, A. Copper-based metal-organic porous materials for CO_2 electrocatalytic reduction to alcohols. *ChemSusChem* **2017**, *10*, 1100-9. DOI PubMed
32. Merino-garcia, I.; Albo, J.; Solla-gullón, J.; Montiel, V.; Irabien, A. Cu oxide/ZnO-based surfaces for a selective ethylene production from gas-phase CO_2 electroconversion. *J. CO2. Util.* **2019**, *31*, 135-42. DOI
33. Nitopi, S.; Bertheussen, E.; Scott, S. B.; et al. Progress and perspectives of electrochemical CO_2 reduction on copper in aqueous electrolyte. *Chem. Rev.* **2019**, *119*, 7610-72. DOI
34. Christensen, O.; Zhao, S.; Sun, Z.; et al. Can the CO_2 reduction reaction be improved on Cu: selectivity and intrinsic activity of functionalized Cu surfaces. *ACS. Catal.* **2022**, *12*, 15737-49. DOI
35. Tomboc, G. M.; Choi, S.; Kwon, T.; Hwang, Y. J.; Lee, K. Potential link between Cu surface and selective CO_2 electroreduction: perspective on future electrocatalyst designs. *Adv. Mater.* **2020**, *32*, e1908398. DOI
36. Hori, Y.; Wakebe, H.; Tsukamoto, T.; Koga, O. Electrocatalytic process of CO selectivity in electrochemical reduction of CO_2 at metal electrodes in aqueous media. *Electrochim. Acta.* **1994**, *39*, 1833-9. DOI
37. Lum, Y.; Cheng, T.; Goddard, W. A. I. I. I.; Ager, J. W. Electrochemical CO reduction builds solvent water into oxygenate products. *J. Am. Chem. Soc.* **2018**, *140*, 9337-40. DOI
38. Feaster, J. T.; Shi, C.; Cave, E. R.; et al. Understanding selectivity for the electrochemical reduction of carbon dioxide to formic acid and carbon monoxide on metal electrodes. *ACS. Catal.* **2017**, *7*, 4822-7. DOI
39. Göttle, A. J.; Koper, M. T. M. Proton-coupled electron transfer in the electrocatalysis of CO_2 reduction: prediction of sequential vs. concerted pathways using DFT. *Chem. Sci.* **2017**, *8*, 458-65. DOI PubMed PMC
40. Han, J.; Bai, X.; Xu, X.; et al. Advances and challenges in the electrochemical reduction of carbon dioxide. *Chem. Sci.* **2024**, *15*, 7870-907. DOI PubMed PMC
41. Li, Y. C.; Wang, Z.; Yuan, T.; et al. Binding site diversity promotes CO_2 electroreduction to ethanol. *J. Am. Chem. Soc.* **2019**, *141*, 8584-91. DOI
42. Farrell, A. E.; Plevin, R. J.; Turner, B. T.; Jones, A. D.; O'Hare, M.; Kammen, D. M. Ethanol can contribute to energy and environmental goals. *Science* **2006**, *311*, 506-8. DOI PubMed
43. Ren, D.; Deng, Y.; Handoko, A. D.; Chen, C. S.; Malkhandi, S.; Yeo, B. S. Selective electrochemical reduction of carbon dioxide to ethylene and ethanol on copper(I) oxide catalysts. *ACS. Catal.* **2015**, *5*, 2814-21. DOI
44. Yang, H.; Li, S.; Xu, Q. Efficient strategies for promoting the electrochemical reduction of CO_2 to C_{2+} products over Cu-based catalysts. *Chin. J. Catal.* **2023**, *48*, 32-65. DOI
45. Wang, Y.; Shen, H.; Livi, K. J. T.; et al. Copper nanocubes for CO_2 reduction in gas diffusion electrodes. *Nano. Lett.* **2019**, *19*, 8461-8. DOI
46. Song, Y.; Peng, R.; Hensley, D. K.; et al. High-selectivity electrochemical conversion of CO_2 to ethanol using a copper nanoparticle/N-doped graphene electrode. *ChemistrySelect* **2016**, *1*, 6055-61. DOI
47. Birdja, Y. Y.; Pérez-gallent, E.; Figueiredo, M. C.; Göttle, A. J.; Calle-vallejo, F.; Koper, M. T. M. Advances and challenges in understanding the electrocatalytic conversion of carbon dioxide to fuels. *Nat. Energy.* **2019**, *4*, 732-45. DOI
48. Roberts, F. S.; Kuhl, K. P.; Nilsson, A. High selectivity for ethylene from carbon dioxide reduction over copper nanocube electrocatalysts. *Angew. Chem. Int. Ed.* **2015**, *54*, 5179-82. DOI PubMed
49. Jiang, K.; Sandberg, R. B.; Akey, A. J.; et al. Metal ion cycling of Cu foil for selective C-C coupling in electrochemical CO_2 reduction. *Nat. Catal.* **2018**, *1*, 111-9. DOI
50. Feijóo, J.; Yang, Y.; Fonseca, G. M. V.; et al. Operando high-energy-resolution X-ray spectroscopy of evolving Cu nanoparticle electrocatalysts for CO_2 reduction. *J. Am. Chem. Soc.* **2023**, *145*, 20208-13. DOI
51. Yin, Z.; Yu, C.; Zhao, Z.; et al. Cu_3N nanocubes for selective electrochemical reduction of CO_2 to ethylene. *Nano. Lett.* **2019**, *19*, 8658-63. DOI
52. Zhou, L.; Li, C.; Lv, J.; et al. Synergistic regulation of hydrophobicity and basicity for copper hydroxide□derived copper to promote the CO_2 electroreduction reaction. *Carbon. Energy.* **2023**, *5*, e328. DOI
53. Su, Y.; Cheng, Y.; Li, Z.; et al. Exploring the impact of nafion modifier on electrocatalytic CO_2 reduction over Cu catalyst. *J. Energy. Chem.* **2024**, *88*, 543-51. DOI
54. Pellessier, J.; Gong, X.; Li, B.; et al. PTFE nanocoating on Cu nanoparticles through dry processing to enhance electrochemical conversion of CO_2 towards multi-carbon products. *J. Mater. Chem. A.* **2023**, *11*, 26252-64. DOI
55. Lin, Y.; Wang, T.; Zhang, L.; et al. Tunable CO_2 electroreduction to ethanol and ethylene with controllable interfacial wettability.

Nat. Commun. **2023**, *14*, 3575. DOI PubMed PMC
56. Rabiee, H.; Ge, L.; Zhao, J.; et al. Regulating the reaction zone of electrochemical CO_2 reduction on gas-diffusion electrodes by distinctive hydrophilic-hydrophobic catalyst layers. *Appl. Catal. B:. Environ.* **2022**, *310*, 121362. DOI
57. Zhang, Y.; Zhang, R.; Chen, F.; et al. Mass-transfer-enhanced hydrophobic Bi microsheets for highly efficient electroreduction of CO_2 to pure formate in a wide potential window. *Appl. Catal. B:. Environ.* **2023**, *322*, 122127. DOI
58. Zhao, T.; Zong, X.; Liu, J.; et al. Functionalizing Cu nanoparticles with fluoric polymer to enhance C_{2+} product selectivity in membraned CO_2 reduction. *Appl. Catal. B:. Environ.* **2024**, *340*, 123281. DOI
59. Reske, R.; Mistry, H.; Behafarid, F.; Roldan, C. B.; Strasser, P. Particle size effects in the catalytic electroreduction of CO_2 on Cu nanoparticles. *J. Am. Chem. Soc.* **2014**, *136*, 6978-86. DOI PubMed
60. Manthiram, K.; Beberwyck, B. J.; Alivisatos, A. P. Enhanced electrochemical methanation of carbon dioxide with a dispersible nanoscale copper catalyst. *J. Am. Chem. Soc.* **2014**, *136*, 13319-25. DOI PubMed
61. Jung, H.; Lee, S. Y.; Lee, C. W.; et al. Electrochemical fragmentation of Cu_2O nanoparticles enhancing selective C-C coupling from CO_2 reduction reaction. *J. Am. Chem. Soc.* **2019**, *141*, 4624-33. DOI
62. Yang, Y.; Louisia, S.; Yu, S.; et al. Operando studies reveal active Cu nanograins for CO_2 electroreduction. *Nature* **2023**, *614*, 262-9. DOI
63. Zhang, J.; My, P. T. H.; Gao, Z.; et al. Electrochemical CO_2 reduction over copper phthalocyanine derived catalysts with enhanced selectivity for multicarbon products. *ACS. Catal.* **2023**, *13*, 9326-35. DOI
64. Zi, X.; Zhou, Y.; Zhu, L.; et al. Breaking K^+ concentration limit on Cu nanoneedles for acidic electrocatalytic CO_2 reduction to multi-carbon products. *Angew. Chem. Int. Ed.* **2023**, *62*, e202309351. DOI
65. Fu, W.; Liu, Z.; Wang, T.; et al. Promoting C_{2+} production from electrochemical CO_2 reduction on shape-controlled cuprous oxide nanocrystals with high-index facets. *ACS. Sustain. Chem. Eng.* **2020**, *8*, 15223-9. DOI
66. Luo, H.; Li, B.; Ma, J. G.; Cheng, P. Surface modification of nano-Cu_2O for controlling CO_2 electrochemical reduction to ethylene and syngas. *Angew. Chem. Int. Ed.* **2022**, *61*, e202116736. DOI
67. Periasamy, A. P.; Ravindranath, R.; Senthil, K. S. M.; Wu, W. P.; Jian, T. R.; Chang, H. T. Facet- and structure-dependent catalytic activity of cuprous oxide/polypyrrole particles towards the efficient reduction of carbon dioxide to methanol. *Nanoscale* **2018**, *10*, 11869-80. DOI PubMed
68. Wu, Q.; Du, R.; Wang, P.; et al. Nanograin-boundary-abundant C_2O-Cu nanocubes with high C_{2+} selectivity and good stability during electrochemical CO_2 reduction at a current density of 500 mA/cm^2. *ACS. Nano.* **2023**, *17*, 12884-94. DOI
69. Geng, Q.; Fan, L.; Chen, H.; et al. Revolutionizing CO_2 electrolysis: fluent gas transportation within hydrophobic porous Cu_2O. *J. Am. Chem. Soc.* **2024**, *146*, 10599-607. DOI
70. Frese, K. W. Electrochemical reduction of CO_2 at solid electrodes. In: Sullivan BP, Krist K, Guard HE, editors. Electrochemical and electrocatalytic reactions of carbon dioxide.Amsterdam: Elsevier; 1993.pp.145-216. DOI
71. Hori, Y.; Takahashi, I.; Koga, O.; Hoshi, N. Electrochemical reduction of carbon dioxide at various series of copper single crystal electrodes. *J. Mol. Catal. A:. Chem.* **2003**, *199*, 39-47. DOI
72. Schouten, K. J.; Qin, Z.; Pérez, G. E.; Koper, M. T. Two pathways for the formation of ethylene in CO reduction on single-crystal copper electrodes. *J. Am. Chem. Soc.* **2012**, *134*, 9864-7. DOI
73. Gao, Y.; Wu, Q.; Liang, X.; et al. Cu_2O nanoparticles with both {100} and {111} facets for enhancing the selectivity and activity of CO_2 electroreduction to ethylene. *Adv. Sci.* **2020**, *7*, 1902820. DOI
74. Wu, Z. Z.; Zhang, X. L.; Niu, Z. Z.; et al. Identification of Cu(100)/Cu(111) interfaces as superior active sites for CO dimerization during CO_2 electroreduction. *J. Am. Chem. Soc.* **2022**, *144*, 259-69. DOI
75. Ma, Z.; Tsounis, C.; Toe, C. Y.; et al. Reconstructing Cu nanoparticle supported on vertical graphene surfaces via electrochemical treatment to tune the selectivity of CO_2 reduction toward valuable products. *ACS. Catal.* **2022**, *12*, 4792-805. DOI
76. Chen, S.; Ye, C.; Wang, Z.; et al. Selective CO_2 reduction to ethylene mediated by adaptive small-molecule engineering of copper-based electrocatalysts. *Angew. Chem. Int. Ed.* **2023**, *62*, e202315621. DOI
77. Liu, B.; Cai, C.; Yang, B.; et al. Intermediate enrichment effect of porous Cu catalyst for CO_2 electroreduction to C2 fuels. *Electrochim. Acta.* **2021**, *388*, 138552. DOI
78. Zhang, J.; Zeng, G.; Zhu, S.; et al. Steering CO_2 electroreduction pathway toward ethanol via surface-bounded hydroxyl species-induced noncovalent interaction. *Proc. Natl. Acad. Sci. U. S. A.* **2023**, *120*, e2218987120. DOI
79. Liu, C.; Zhang, M.; Li, J.; et al. Nanoconfinement engineering over hollow multi-shell structured copper towards efficient electrocatalytical C-C coupling. *Angew. Chem. Int. Ed.* **2022**, *61*, e202113498. DOI
80. Yang, P. P.; Zhang, X. L.; Gao, F. Y.; et al. Protecting copper oxidation state via intermediate confinement for selective CO_2 electroreduction to C_{2+} fuels. *J. Am. Chem. Soc.* **2020**, *142*, 6400-8. DOI
81. Chen, X.; Chen, J.; Alghoraibi, N. M.; et al. Electrochemical CO_2-to-ethylene conversion on polyamine-incorporated Cu electrodes. *Nat. Catal.* **2021**, *4*, 20-7. DOI
82. Wakerley, D.; Lamaison, S.; Ozanam, F.; et al. Bio-inspired hydrophobicity promotes CO_2 reduction on a Cu surface. *Nat. Mater.* **2019**, *18*, 1222-7. DOI
83. Qu, Y.; Li, Z.; Chen, W.; et al. Direct transformation of bulk copper into copper single sites via emitting and trapping of atoms. *Nat. Catal.* **2018**, *1*, 781-6. DOI
84. Lang, R.; Du, X.; Huang, Y.; et al. Single-atom catalysts based on the metal-oxide interaction. *Chem. Rev.* **2020**, *120*, 11986-2043.

DOI

85. Ji, S.; Chen, Y.; Wang, X.; Zhang, Z.; Wang, D.; Li, Y. Chemical synthesis of single atomic site catalysts. *Chem. Rev.* **2020**, *120*, 11900-55. DOI
86. Zhao, Z.; Lu, G. Cu-based single-atom catalysts boost electroreduction of CO_2 to CH_3OH: first-principles predictions. *J. Phys. Chem. C.* **2019**, *123*, 4380-7. DOI
87. Cai, Y.; Fu, J.; Zhou, Y.; et al. Insights on forming N,O-coordinated Cu single-atom catalysts for electrochemical reduction CO_2 to methane. *Nat. Commun.* **2021**, *12*, 586. DOI PubMed PMC
88. Li, Z.; Qiu, S.; Song, Y.; et al. Engineering single-atom active sites anchored covalent organic frameworks for efficient metallaphotoredox CN cross-coupling reactions. *Sci. Bull.* **2022**, *67*, 1971-81. DOI
89. Li, X.; Yu, X.; Yu, Q. Research progress on electrochemical CO_2 reduction for Cu-based single-atom catalysts. *Sci. China. Mater.* **2023**, *66*, 3765-81. DOI
90. Li, X.; Rong, H.; Zhang, J.; Wang, D.; Li, Y. Modulating the local coordination environment of single-atom catalysts for enhanced catalytic performance. *Nano. Res.* **2020**, *13*, 1842-55. DOI
91. Zhu, Y.; Sokolowski, J.; Song, X.; He, Y.; Mei, Y.; Wu, G. Engineering local coordination environments of atomically dispersed and heteroatom-coordinated single metal site electrocatalysts for clean energy-conversion. *Adv. Energy. Mater.* **2020**, *10*, 1902844. DOI
92. Dong, J.; Liu, Y.; Pei, J.; et al. Continuous electroproduction of formate via CO_2 reduction on local symmetry-broken single-atom catalysts. *Nat. Commun.* **2023**, *14*, 6849. DOI PubMed PMC
93. Wang, X.; Ju, W.; Liang, L.; et al. Electrochemical CO_2 activation and valorization on metallic copper and carbon-embedded N-coordinated single metal MNC catalysts. *Angew. Chem. Int. Ed.* **2024**, *63*, e202401821. DOI
94. Han, L.; Song, S.; Liu, M.; et al. Stable and efficient single-atom Zn catalyst for CO_2 reduction to CH_4. *J. Am. Chem. Soc.* **2020**, *142*, 12563-7. DOI
95. Zhao, J.; Chen, Z.; Zhao, J. Metal-free graphdiyne doped with sp-hybridized boron and nitrogen atoms at acetylenic sites for high-efficiency electroreduction of CO_2 to CH_4 and C_2H_4. *J. Mater. Chem. A.* **2019**, *7*, 4026-35. DOI
96. He, F.; Zhuang, J.; Lu, B.; et al. Ni-based catalysts derived from Ni-Zr-Al ternary hydrotalcites show outstanding catalytic properties for low-temperature CO_2 methanation. *Appl. Catal. B:. Environ.* **2021**, *293*, 120218. DOI
97. Liu, X.; Wang, Z.; Tian, Y.; Zhao, J. Graphdiyne-supported single iron atom: a promising electrocatalyst for carbon dioxide electroreduction into methane and ethanol. *J. Phys. Chem. C.* **2020**, *124*, 3722-30. DOI
98. Zhao, P.; Jiang, H.; Shen, H.; et al. Construction of low-coordination Cu-C_2 single-atoms electrocatalyst facilitating the efficient electrochemical CO_2 reduction to methane. *Angew. Chem. Int. Ed.* **2023**, *62*, e202314121. DOI
99. Shi, G.; Xie, Y.; Du, L.; et al. Constructing Cu-C bonds in a graphdiyne-regulated Cu single-atom electrocatalyst for CO_2 reduction to CH_4. *Angew. Chem. Int. Ed.* **2022**, *61*, e202203569. DOI
100. Li, M.; Zhang, F.; Kuang, M.; et al. Atomic Cu sites engineering enables efficient CO_2 electroreduction to methane with high CH_4/C_2H_4 ratio. *Nanomicro. Lett.* **2023**, *15*, 238. DOI PubMed PMC
101. Chen, S.; Li, Y.; Bu, Z.; et al. Boosting CO_2-to-CO conversion on a robust single-atom copper decorated carbon catalyst by enhancing intermediate binding strength. *J. Mater. Chem. A.* **2021**, *9*, 1705-12. DOI
102. Chen, S.; Xia, M.; Zhang, X.; et al. Guanosine-derived atomically dispersed Cu-N_3-C sites for efficient electroreduction of carbon dioxide. *J. Colloid. Interface. Sci.* **2023**, *646*, 863-71. DOI
103. Purbia, R.; Choi, S. Y.; Woo, C. H.; et al. Highly selective and low-overpotential electrocatalytic CO_2 reduction to ethanol by Cu-single atoms decorated N-doped carbon dots. *Appl. Catal. B:. Environ.* **2024**, *345*, 123694. DOI
104. Pan, F.; Fang, L.; Li, B.; et al. N and OH-immobilized Cu_3 clusters in situ reconstructed from single-metal sites for efficient CO_2 electromethanation in bicontinuous mesochannels. *J. Am. Chem. Soc.* **2024**, *146*, 1423-34. DOI
105. Xia, W.; Xie, Y.; Jia, S.; et al. Adjacent copper single atoms promote C-C coupling in electrochemical CO_2 reduction for the efficient conversion of ethanol. *J. Am. Chem. Soc.* **2023**, *145*, 17253-64. DOI
106. Xu, C.; Zhi, X.; Vasileff, A.; et al. Highly selective two-electron electrocatalytic CO_2 reduction on single-atom Cu catalysts. *Small. Struct.* **2021**, *2*, 2000058. DOI
107. Cheng, H.; Wu, X.; Li, X.; et al. Construction of atomically dispersed Cu-N_4 sites via engineered coordination environment for high-efficient CO_2 electroreduction. *Chem. Eng. J.* **2021**, *407*, 126842. DOI
108. Karapinar, D.; Huan, N. T.; Ranjbar, S. N.; et al. Electroreduction of CO_2 on single-site copper-nitrogen-doped carbon material: selective formation of ethanol and reversible restructuration of the metal sites. *Angew. Chem. Int. Ed.* **2019**, *58*, 15098-103. DOI
109. Zhao, K.; Nie, X.; Wang, H.; et al. Selective electroreduction of CO_2 to acetone by single copper atoms anchored on N-doped porous carbon. *Nat. Commun.* **2020**, *11*, 2455. DOI PubMed PMC
110. Roy, S.; Li, Z.; Chen, Z.; et al. Cooperative copper single-atom catalyst in 2D carbon nitride for enhanced CO_2 electrolysis to methane. *Adv. Mater.* **2024**, *36*, e2300713. DOI
111. Wu, Q. J.; Si, D. H.; Sun, P. P.; et al. Atomically precise copper nanoclusters for highly efficient electroreduction of CO_2 towards hydrocarbons via breaking the coordination symmetry of Cu site. *Angew. Chem. Int. Ed.* **2023**, *62*, e202306822. DOI
112. Lv, Z.; Wang, C.; Liu, Y.; et al. Improving CO_2-to-C_2 conversion of atomic CuFONC electrocatalysts through F, O-codrived optimization of local coordination environment. *Adv. Energy. Mater.* **2024**, *14*, 2400057. DOI
113. Chen, C.; Li, Y.; Yu, S.; et al. Cu-Ag tandem catalysts for high-rate CO_2 electrolysis toward multicarbons. *Joule* **2020**, *4*, 1688-99. DOI

114. Shen, S.; Peng, X.; Song, L.; et al. AuCu alloy nanoparticle embedded Cu submicrocone arrays for selective conversion of CO_2 to ethanol. *Small* **2019**, *15*, e1902229. DOI
115. Cao, B.; Li, F.; Gu, J. Designing Cu-based tandem catalysts for CO_2 electroreduction based on mass transport of CO intermediate. *ACS. Catal.* **2022**, *12*, 9735-52. DOI
116. Ji, Y.; Guan, A.; Zheng, G. Copper-based catalysts for electrochemical carbon monoxide reduction. *Cell. Rep. Phys. Sci.* **2022**, *3*, 101072. DOI
117. Luc, W.; Collins, C.; Wang, S.; et al. Ag-Sn bimetallic catalyst with a core-shell structure for CO_2 reduction. *J. Am. Chem. Soc.* **2017**, *139*, 1885-93. DOI
118. Ross, M. B.; Dinh, C. T.; Li, Y.; et al. Tunable Cu enrichment enables designer syngas electrosynthesis from CO_2. *J. Am. Chem. Soc.* **2017**, *139*, 9359-63. DOI
119. Peng, L.; Wang, Y.; Wang, Y.; et al. Separated growth of Bi-Cu bimetallic electrocatalysts on defective copper foam for highly converting CO_2 to formate with alkaline anion-exchange membrane beyond $KHCO_3$ electrolyte. *Appl. Catal. B:. Environ.* **2021**, *288*, 120003. DOI
120. Hou, C.; Wang, H.; Li, C.; Xu, Q. From metal-organic frameworks to single/dual-atom and cluster metal catalysts for energy applications. *Energy. Environ. Sci.* **2020**, *13*, 1658-93. DOI
121. Xu, Y.; Li, C.; Xiao, Y.; et al. Tuning the selectivity of liquid products of CO_2RR by Cu-Ag alloying. *ACS. Appl. Mater. Interfaces.* **2022**, *14*, 11567-74. DOI
122. Yang, Z.; Wang, H.; Fei, X.; et al. MOF derived bimetallic CuBi catalysts with ultra-wide potential window for high-efficient electrochemical reduction of CO_2 to formate. *Appl. Catal. B:. Environ.* **2021**, *298*, 120571. DOI
123. Hoang, T. T. H.; Verma, S.; Ma, S.; et al. Nanoporous copper-silver alloys by additive-controlled electrodeposition for the selective electroreduction of CO_2 to ethylene and ethanol. *J. Am. Chem. Soc.* **2018**, *140*, 5791-7. DOI
124. Ouyang, Y.; Shi, L.; Bai, X.; Ling, C.; Li, Q.; Wang, J. Selectivity of electrochemical CO_2 reduction toward ethanol and ethylene: the key role of surface-active hydrogen. *ACS. Catal.* **2023**, *13*, 15448-56. DOI
125. Morales-guio, C. G.; Cave, E. R.; Nitopi, S. A.; et al. Improved CO_2 reduction activity towards C_{2+} alcohols on a tandem gold on copper electrocatalyst. *Nat. Catal.* **2018**, *1*, 764-71. DOI
126. Wei, Z.; Yue, S.; Gao, S.; Cao, M.; Cao, R. Synergetic effects of gold-doped copper nanowires with low Au content for enhanced electrocatalytic CO_2 reduction to multicarbon products. *Nano. Res.* **2023**, *16*, 7777-83. DOI
127. Zheng, Y.; Zhang, J.; Ma, Z.; et al. Seeded growth of gold-copper janus nanostructures as a tandem catalyst for efficient electroreduction of CO_2 to C_{2+} products. *Small* **2022**, *18*, e2201695. DOI
128. Ma, Y.; Yu, J.; Sun, M.; et al. Confined growth of silver-copper janus nanostructures with {100} facets for highly selective tandem electrocatalytic carbon dioxide reduction. *Adv. Mater.* **2022**, *34*, e2110607. DOI
129. Wei, C.; Yang, Y.; Ma, H.; et al. Nanoscale management of CO transport in CO_2 electroreduction: boosting faradaic efficiency to multicarbon products via nanostructured tandem electrocatalysts. *Adv. Funct. Mater.* **2023**, *33*, 2214992. DOI
130. Choi, C.; Cai, J.; Lee, C.; Lee, H. M.; Xu, M.; Huang, Y. Intimate atomic Cu-Ag interfaces for high CO_2RR selectivity towards CH_4 at low over potential. *Nano. Res.* **2021**, *14*, 3497-501. DOI
131. Li, P.; Bi, J.; Liu, J.; et al. In situ dual doping for constructing efficient CO_2-to-methanol electrocatalysts. *Nat. Commun.* **2022**, *13*, 1965. DOI PubMed PMC
132. Du, C.; Mills, J. P.; Yohannes, A. G.; et al. Cascade electrocatalysis via AgCu single-atom alloy and Ag nanoparticles in CO_2 electroreduction toward multicarbon products. *Nat. Commun.* **2023**, *14*, 6142. DOI PubMed PMC
133. Qi, K.; Zhang, Y.; Onofrio, N.; et al. Unlocking direct CO_2 electrolysis to C_3 products via electrolyte supersaturation. *Nat. Catal.* **2023**, *6*, 319-31. DOI
134. Li, J.; Chen, Y.; Yao, B.; et al. Cascade dual sites modulate local CO coverage and hydrogen-binding strength to boost CO_2 electroreduction to ethylene. *J. Am. Chem. Soc.* **2024**, *146*, 5693-701. DOI
135. Kattel, S.; Ramírez, P. J.; Chen, J. G.; Rodriguez, J. A.; Liu, P. Active sites for CO_2 hydrogenation to methanol on Cu/ZnO catalysts. *Science* **2017**, *355*, 1296-99. DOI
136. Zhu, J.; Ciolca, D.; Liu, L.; Parastaev, A.; Kosinov, N.; Hensen, E. J. M. Flame synthesis of Cu/ZnO-CeO_2 catalysts: synergistic metal-support interactions promote CH_3OH selectivity in CO_2 hydrogenation. *ACS. Catal.* **2021**, *11*, 4880-92. DOI
137. Amann, P.; Klötzer, B.; Degerman, D.; et al. The state of zinc in methanol synthesis over a Zn/ZnO/Cu(211) model catalyst. *Science* **2022**, *376*, 603-8. DOI
138. Wan, L.; Zhang, X.; Cheng, J.; et al. Bimetallic Cu-Zn catalysts for electrochemical CO_2 reduction: phase-separated versus core-shell distribution. *ACS. Catal.* **2022**, *12*, 2741-8. DOI
139. Zhen, S.; Zhang, G.; Cheng, D.; et al. Nature of the active sites of copper zinc catalysts for carbon dioxide electroreduction. *Angew. Chem. Int. Ed.* **2022**, *61*, e202201913. DOI
140. Zhang, Z.; Tian, H.; Bian, L.; Liu, S.; Liu, Y.; Wang, Z. Cu-Zn-based alloy/oxide interfaces for enhanced electroreduction of CO_2 to C_{2+} products. *J. Energy. Chem.* **2023**, *83*, 90-7. DOI
141. Liu, M.; Wang, Q.; Luo, T.; et al. Potential alignment in tandem catalysts enhances CO_2-to-C_2H_4 conversion efficiencies. *J. Am. Chem. Soc.* **2024**, *146*, 468-75. DOI
142. Song, J.; Zhang, H.; Sun, R.; et al. Local CO generator enabled by a CO-producing core for kinetically enhancing electrochemical CO_2 reduction to multicarbon products. *ACS. Nano.* **2024**, *18*, 11416-24. DOI

143. Wei, B.; Xiong, Y.; Zhang, Z.; Hao, J.; Li, L.; Shi, W. Efficient electrocatalytic reduction of CO_2 to HCOOH by bimetallic In-Cu nanoparticles with controlled growth facet. *Appl. Catal. B:. Environ.* **2021**, *283*, 119646. DOI
144. Wang, Z.; Li, Z.; Liu, S.; et al. Enhancing the selectivity of CO_2-to-HCOOH conversion by constructing tensile-strained Cu catalyst. *Mater. Today. Phys.* **2023**, *38*, 101247. DOI
145. Li, X.; Qin, M.; Wu, X.; et al. Enhanced CO affinity on Cu facilitates CO_2 electroreduction toward multi-carbon products. *Small* **2023**, *19*, e2302530. DOI
146. Zheng, T.; Liu, C.; Guo, C.; et al. Copper-catalysed exclusive CO_2 to pure formic acid conversion via single-atom alloying. *Nat. Nanotechnol.* **2021**, *16*, 1386-93. DOI
147. Cao, Y.; Chen, S.; Bo, S.; et al. Single atom Bi decorated copper alloy enables C-C coupling for electrocatalytic reduction of CO_2 into C_{2+} products. *Angew. Chem. Int. Ed.* **2023**, *62*, e202303048. DOI
148. Hu, S.; Chen, Y.; Zhang, Z.; et al. Ampere-level current density CO_2 reduction with high C_{2+} selectivity on $La(OH)_3$-modified Cu catalysts. *Small* **2024**, *20*, e2308226. DOI
149. Li, P.; Bi, J.; Liu, J.; et al. p-d orbital hybridization induced by p-block metal-doped Cu promotes the formation of C_{2+} products in ampere-level CO_2 electroreduction. *J. Am. Chem. Soc.* **2023**, *145*, 4675-82. DOI
150. Xie, M.; Shen, Y.; Ma, W.; et al. Fast screening for copper-based bimetallic electrocatalysts: efficient electrocatalytic reduction of CO_2 to C_{2+} products on magnesium-modified copper. *Angew. Chem. Int. Ed.* **2022**, *61*, e202213423. DOI
151. Hao, J.; Zhu, H.; Li, Y.; et al. Tuning the electronic structure of AuNi homogeneous solid-solution alloy with positively charged Ni center for highly selective electrochemical CO_2 reduction. *Chem. Eng. J.* **2021**, *404*, 126523. DOI
152. Liu, A.; Yang, Y.; Ren, X.; et al. Current progress of electrocatalysts for ammonia synthesis through electrochemical nitrogen reduction under ambient conditions. *ChemSusChem* **2020**, *13*, 3766-88. DOI
153. Xu, H.; Rebollar, D.; He, H.; et al. Highly selective electrocatalytic CO_2 reduction to ethanol by metallic clusters dynamically formed from atomically dispersed copper. *Nat. Energy.* **2020**, *5*, 623-32. DOI
154. Pan, F.; Yang, X.; O'carroll, T.; Li, H.; Chen, K.; Wu, G. Carbon catalysts for electrochemical CO_2 reduction toward multicarbon products. *Adv. Energy. Mater.* **2022**, *12*, 2200586. DOI
155. Yan, Y.; Ke, L.; Ding, Y.; et al. Recent advances in Cu-based catalysts for electroreduction of carbon dioxide. *Mater. Chem. Front.* **2021**, *5*, 2668-83. DOI
156. Su, X.; Wang, C.; Zhao, F.; Wei, T.; Zhao, D.; Zhang, J. Size effects of supported Cu-based catalysts for the electrocatalytic CO_2 reduction reaction. *J. Mater. Chem. A.* **2023**, *11*, 23188-210. DOI
157. Yang, H.; Wu, Y.; Li, G.; et al. Scalable production of efficient single-atom copper decorated carbon membranes for CO_2 electroreduction to methanol. *J. Am. Chem. Soc.* **2019**, *141*, 12717-23. DOI
158. Wu, Y.; Jiang, Z.; Lu, X.; Liang, Y.; Wang, H. Domino electroreduction of CO_2 to methanol on a molecular catalyst. *Nature* **2019**, *575*, 639-42. DOI
159. Zheng, W.; Yang, J.; Chen, H.; et al. Atomically defined undercoordinated active sites for highly efficient CO_2 electroreduction. *Adv. Funct. Mater.* **2020**, *30*, 1907658. DOI
160. Feng, Z.; Tang, Y.; Ma, Y.; et al. Theoretical investigation of CO_2 electroreduction on N (B)-doped graphdiyne mononlayer supported single copper atom. *Appl. Surf. Sci.* **2021**, *538*, 148145. DOI
161. Xu, F.; Feng, B.; Shen, Z.; et al. Oxygen-bridged Cu binuclear sites for efficient electrocatalytic CO_2 reduction to ethanol at ultralow overpotential. *J. Am. Chem. Soc.* **2024**, *146*, 9365-74. DOI
162. Jiao, Y.; Zheng, Y.; Chen, P.; Jaroniec, M.; Qiao, S. Z. Molecular scaffolding strategy with synergistic active centers to facilitate electrocatalytic CO_2 reduction to hydrocarbon/alcohol. *J. Am. Chem. Soc.* **2017**, *139*, 18093-100. DOI
163. Li, H.; Cao, S.; Sun, H.; et al. CuNCN derived Cu-based/CxNy catalysts for highly selective CO_2 electroreduction to hydrocarbons. *Appl. Catal. B:. Environ.* **2023**, *320*, 121948. DOI
164. Li, Q.; Zhu, W.; Fu, J.; Zhang, H.; Wu, G.; Sun, S. Controlled assembly of Cu nanoparticles on pyridinic-N rich graphene for electrochemical reduction of CO_2 to ethylene. *Nano. Energy.* **2016**, *24*, 1-9. DOI
165. Waugh, K. Methanol synthesis. *Catal. Today.* **1992**, *15*, 51-75. DOI
166. Chen, S.; Abdel-Mageed, A. M.; Dyballa, M.; et al. Raising the CO_x methanation activity of a $Ru/_{\gamma}$-Al_2O_3 catalyst by activated modification of metal-support interactions. *Angew. Chem. Int. Ed.* **2020**, *59*, 22763-70. DOI
167. Chen, J.; Falivene, L.; Caporaso, L.; Cavallo, L.; Chen, E. Y. Selective reduction of CO_2 to CH_4 by tandem hydrosilylation with mixed Al/B catalysts. *J. Am. Chem. Soc.* **2016**, *138*, 5321-33. DOI PubMed
168. Sampson, M. D.; Kubiak, C. P. Manganese electrocatalysts with bulky bipyridine ligands: utilizing lewis acids to promote carbon dioxide reduction at low overpotentials. *J. Am. Chem. Soc.* **2016**, *138*, 1386-93. DOI
169. Kim, Y. E.; Kim, J.; Lee, Y. Formation of a nickel carbon dioxide adduct and its transformation mediated by a lewis acid. *Chem. Commun.* **2014**, *50*, 11458-61. DOI
170. Chen, S.; Wang, B.; Zhu, J.; et al. Lewis acid site-promoted single-atomic Cu catalyzes electrochemical CO_2 methanation. *Nano. Lett.* **2021**, *21*, 7325-31. DOI
171. Yuan, J.; Zhang, J.; Yang, M.; Meng, W.; Wang, H.; Lu, J. CuO nanoparticles supported on TiO_2 with high efficiency for CO_2 electrochemical reduction to ethanol. *Catalysts* **2018**, *8*, 171. DOI
172. Chu, D.; Qin, G.; Yuan, X.; Xu, M.; Zheng, P.; Lu, J. Fixation of CO_2 by electrocatalytic reduction and electropolymerization in ionic liquid-H_2O solution. *ChemSusChem* **2008**, *1*, 205-9. DOI

173. Thompson, T. L.; Diwald, O.; Yates, J. T. CO_2 as a probe for monitoring the surface defects on TiO_2(110)-temperature-programmed desorption. *J. Phys. Chem. B.* **2003**, *107*, 11700-4. DOI
174. Cueto, L. F.; Hirata, G. A.; Sánchez, E. M. Thin-film TiO_2 electrode surface characterization upon CO_2 reduction processes. *J. Sol-Gel. Sci. Technol.* **2006**, *37*, 105-9. DOI
175. Abdinejad, M.; Subramanian, S.; Motlagh, M. K.; et al. Insertion of MXene-based materials into Cu-Pd 3D aerogels for electroreduction of CO_2 to formate. *Adv. Energy. Mater.* **2023**, *13*, 2300402. DOI
176. Lin, L.; Liu, T.; Xiao, J.; et al. Enhancing CO_2 electroreduction to methane with a cobalt phthalocyanine and zinc-nitrogen-carbon tandem catalyst. *Angew. Chem. Int. Ed.* **2020**, *59*, 22408-13. DOI
177. Chen, S.; Li, W. H.; Jiang, W.; et al. MOF encapsulating N-heterocyclic carbene-ligated copper single-atom site catalyst towards efficient methane electrosynthesis. *Angew. Chem. Int. Ed.* **2022**, *61*, e202114450. DOI